The Astrophysical Journal, 979:176 (20pp), 2025 February 1 https://doi.org/10.3847/1538-4357/ad9b0c

A Pride of Satellites in the Constellation Leo? Discovery of the Leo VI Milky Way Satellite Ultra-faint Dwarf Galaxy with DELVE Early Data Release 3

C. Y. Tan[1,2], W. Cerny[3], A. Drlica-Wagner[1,4,5], A. B. Pace[6], M. Geha[3], A. P. Ji[1,5], T. S. Li[7], M. Adamów[8], D. Anbajagane[1,5], C. R. Bom[9], J. A. Carballo-Bello[10], J. L. Carlin[11], C. Chang[1,5], A. Chaturvedi[12], A. Chiti[1,5], Y. Choi[13], M. L. M. Collins[12], A. Doliva-Dolinsky[14,15], P. S. Ferguson[16], R. A. Gruendl[8,17], D. J. James[18,19], G. Limberg[1,20], M. Navabi[12], D. Martínez-Delgado[21], C. E. Martínez-Vázquez[22], G. E. Medina[7], B. Mutlu-Pakdil[15], D. L. Nidever[13,23], N. E. D. Noël[12], A. H. Riley[24], J. D. Sakowska[12], D. J. Sand[25], J. Sharp[5], G. S. Stringfellow[26], C. Tolley[27], D. L. Tucker[4], and A. K. Vivas[28]
(DELVE Collaboration)
[1] Kavli Institute for Cosmological Physics, University of Chicago, Chicago, IL 60637, USA; chinyi@uchicago.edu
[2] Department of Physics, University of Chicago, Chicago, IL 60637, USA
[3] Department of Astronomy, Yale University, New Haven, CT 06520, USA
[4] Fermi National Accelerator Laboratory, P.O. Box 500, Batavia, IL 60510, USA
[5] Department of Astronomy and Astrophysics, University of Chicago, Chicago, IL 60637, USA
[6] McWilliams Center for Cosmology & Astrophysics, Carnegie Mellon University, 5000 Forbes Ave, Pittsburgh, PA 15213, USA
[7] Department of Astronomy and Astrophysics, University of Toronto, 50 St. George Street, Toronto, ON M5S 3H4, Canada
[8] Center for Astrophysical Surveys, National Center for Supercomputing Applications, 1205 West Clark St., Urbana, IL 61801, USA
[9] Centro Brasileiro de Pesquisas Físicas, Rua Dr. Xavier Sigaud 150, 22290-180 Rio de Janeiro, RJ, Brazil
[10] Instituto de Alta Investigación, Universidad de Tarapacá, Casilla 7D, Arica, Chile
[11] Rubin Observatory/AURA, 950 North Cherry Avenue, Tucson, AZ 85719, USA
[12] Department of Physics, University of Surrey, Guildford, GU2 7XH, UK
[13] NSF NOIRLab, 950 N. Cherry Ave., Tucson, AZ 85719, USA
[14] Department of Chemistry and Physics, University of Tampa, 401 West Kennedy Boulevard, Tampa, FL 33606, USA
[15] Department of Physics and Astronomy, Dartmouth College, Hanover, NH 03755, USA
[16] Department of Physics, University of Wisconsin-Madison, Madison, WI 53706, USA
[17] Department of Astronomy, University of Illinois, 1002 W. Green Street, Urbana, IL 61801, USA
[18] ASTRAVEO LLC, PO Box 1668, Gloucester, MA 01931, USA
[19] Applied Materials Inc., 35 Dory Road, Gloucester, MA 01930, USA
[20] Universidade de São Paulo, IAG, Departamento de Astronomia, SP 05508-090, São Paulo, Brazil
[21] Instituto de Astrofísica de Andalucía, CSIC, E-18080 Granada, Spain
[22] International Gemini Observatory/NSF NOIRLab, 670 N. A'ohoku Place, Hilo, HI 96720, USA
[23] Department of Physics, Montana State University, P.O. Box 173840, Bozeman, MT 59717-3840, USA
[24] Institute for Computational Cosmology, Department of Physics, Durham University, South Road, Durham, DH1 3LE, UK
[25] Department of Astronomy, Steward Observatory, 933 North Cherry Avenue, Room N204, Tucson, AZ 85721-0065, USA
[26] Center for Astrophysics and Space Astronomy, University of Colorado, 389 UCB, Boulder, CO 80309-0389, USA
[27] Department of Astronomy, University of California, Berkeley, CA 94720-3411, USA
[28] Cerro Tololo Inter-American Observatory, NSF NOIRLab, Casilla 603, La Serena, Chile
Received 2024 August 7; revised 2024 November 11; accepted 2024 December 3; published 2025 January 24

Abstract

We report the discovery and spectroscopic confirmation of an ultra-faint Milky Way satellite in the constellation of Leo. This system was discovered as a spatial overdensity of resolved stars observed with Dark Energy Camera (DECam) data from an early version of the third data release of the DECam Local Volume Exploration (or DELVE) survey. The low luminosity ($M_V = -3.56^{+0.47}_{-0.37}$; $L_V = 2300^{+1200}_{-700} L_\odot$), large size ($R_{l/2} = 90^{+30}_{-30}$ pc), and large heliocentric distance ($D = 111^{+9}_{-6}$ kpc) are all consistent with the population of ultra-faint dwarf galaxies (UFDs). Using Keck/DEIMOS observations of the system, we were able to spectroscopically confirm nine member stars, while measuring a tentative mass-to-light ratio of $700^{+1400}_{-500} M_\odot/L_\odot$ and a nonzero metallicity dispersion of $\sigma_{[Fe/H]} = 0.19^{+0.14}_{-0.11}$, further confirming Leo VI's identity as a UFD. While the system has a highly elliptical shape, $\epsilon = 0.54^{+0.19}_{-0.29}$, we do not find any conclusive evidence that it is tidally disrupting. Moreover, despite the apparent on-sky proximity of Leo VI to members of the proposed Crater-Leo infall group, its smaller heliocentric distance and inconsistent position in energy–angular momentum space make it unlikely that Leo VI is part of the proposed infall group.

Unified Astronomy Thesaurus concepts: Dwarf galaxies (416); Surveys (1671)

1. Introduction

Ultra-faint dwarf galaxies (UFDs) are among the oldest, faintest ($M_V \gtrsim -7.7$; $L_V \lesssim 10^5\ L_\odot$), most metal-poor ([Fe/H] $\lesssim -2$), and most dark-matter-dominated ($M_\odot/L_\odot > 100$) stellar systems known (J. D. Simon 2019). UFDs were first discovered in the Sloan Digital Sky Survey (SDSS; B. Willman et al. 2005a, 2005b) following the advent of CCD-based digital sky surveys. Subsequently, more recent surveys such as Pan-STARRS 1 (PS1; K. C. Chambers et al. 2016), the Dark Energy Survey (DES; Dark Energy Survey Collaboration et al. 2016), and the Dark Energy Camera (DECam) Local Volume Exploration Survey (DELVE; A. Drlica-Wagner et al. 2021) have drastically expanded the known population of these faint resolved systems

around the Milky Way (MW) to more than 60 systems (e.g., K. Bechtol et al. 2015; A. Drlica-Wagner et al. 2015, 2020; S. E. Koposov et al. 2015; B. P. M. Laevens et al. 2015; S. Mau et al. 2020; W. Cerny et al. 2023b).

The high dark matter content of UFDs makes them excellent laboratories for understanding the nature of dark matter. For example, the luminosity function of UFDs and their density profiles depend sensitively on the dark matter particle mass, thermal history, and self-interaction cross section (e.g., M. Rocha et al. 2013; M. R. Lovell et al. 2014; M. Kaplinghat et al. 2016; J. S. Bullock & M. Boylan-Kolchin 2017). Their internal dynamics are also sensitive to weak heating effects from the dark matter halo, allowing for potentially measurable effects on their stellar components (T. D. Brandt 2016; J. Peñarrubia et al. 2016). UFDs are also excellent targets to search for standard model products coming from dark matter annihilation or decay due to their proximity, high dark matter content, and lack of high-energy astrophysical backgrounds (e.g., M. Ackermann et al. 2015; V. Bonnivard et al. 2015; A. Geringer-Sameth et al. 2015b; A. McDaniel et al. 2023; K. K. Boddy et al. 2024). Furthermore, the study of individual UFDs can yield insights into the processes of satellite accretion and tidal disruption around MW-mass host galaxies. Due to their low luminosities, most of the UFD systems discovered thus far are resolved satellites of the MW and other nearby galaxies in the Local Volume (see J. D. Simon 2019, and references therein).

In this paper, we present the discovery and confirmation of the UFD Leo VI, a low-luminosity, metal-poor MW satellite located at a heliocentric distance of ∼110 kpc. The paper also acts as an reference for the DELVE Early Data Release 3 (EDR3) data set used to discover the system, which we describe in detail in Section 2. We use Section 3 to describe the matched-filter search methods used to discover Leo VI in DELVE EDR3 and Section 4 to present system's morphological properties obtained from follow-up DECam observations. In Section 5, we describe the line-of-sight velocity and metallicity measurements of the member stars of Leo VI obtained through follow-up Keck/DEep Imaging Multi-Object Spectrograph (DEIMOS) data. We then discuss whether Leo VI could be tidally disrupting as well as its potential associations with other Local Group systems in Section 6 and summarize our results in Section 7.

2. DELVE Early Data Release 3

DELVE is an ongoing observing program that uses DECam (B. Flaugher et al. 2015) on the 4 m Blanco Telescope at the Cerro Tololo Inter-American Observatory (CTIO) in Chile to contiguously image the high Galactic latitude southern sky in the g, r, i, and z bands (A. Drlica-Wagner et al. 2021, 2022). To date, DELVE has been allocated more than 150 nights to pursue three observational programs dedicated to studying ultra-faint satellite galaxies around the MW (DELVE–WIDE), the Magellanic Clouds (DELVE–MC), and Magellanic analogs in the Local Volume (DELVE–DEEP). New DECam observations and public archival DECam data are self-consistently processed using the DES Data Management (DESDM) pipeline (E. Morganson et al. 2018).

The forthcoming DELVE DR3 combines exposures from DELVE with other public DECam programs such as DES and the DECam Legacy Survey (DECaLS; A. Dey et al. 2019). Compared to the previous DELVE data release, the exposures were coadded to improve the depth and precision of photometric measurements. In this analysis, we use an object catalog from DELVE EDR3, which is an early internal version of the third DELVE data release containing only exposures in the northern Galactic cap ($b > 10°$). While DELVE EDR3 is an internal data release, the full DELVE DR3 follows the same processing procedure and will be made publicly available in the future.

The DELVE EDR3 data were self-consistently processed using the DESDM pipeline in the context of the DECam All Data Everywhere program at the National Center for Supercomputing Applications. The configuration of the DESDM image detrending and coaddition pipeline closely follows the pipeline used to produce DES Data Release 2 (DR2; T. M. C. Abbott et al. 2021). We briefly summarize key aspects of the DESDM pipeline used to produce DELVE EDR3 here.

Processing of individual DECam exposures was performed following the "Final Cut" pipeline described in E. Morganson et al. (2018). All exposures go through a preprocessing step, which includes cross talk and overscan correction as well as bad pixel masking for each DECam CCD. In addition, we correct for the CCD nonlinearity with CCD-dependent lookup tables that convert the observed flux to the fitted model (G. M. Bernstein et al. 2017). Around bright sources, charges accumulating on strongly illuminated pixels will repel nearby charges, broadening the source's point-spread function (PSF) in a phenomenon known as the "brighter–fatter effect" (e.g., P. Antilogus et al. 2014). To account for this effect, we use a CCD-dependent kernel derived from early DECam data by D. Gruen et al. (2015). We then apply flat-field corrections using the raw, bias, dome flats, amplifier-specific conversion, and the nonlinear correction to each CCD. For the bias and dome flat images, we used a set of "supercals" assembled for DES by combining bias and flats taken over several nights (see Section 3.2 of E. Morganson et al. 2018). The bias, dome flat images, and other image calibration data products were used corresponding to the nearest DES observing epoch.

At the time of observations, a world coordinate system (WCS) was added to the image using the optical axis read from the telescope encoders and a fixed distortion map derived from the star flats. The WCS is then updated with an initial single-exposure astrometric solution calculated using `SCAMP` (E. Bertin 2006), with Gaia DR2 (Gaia Collaboration et al. 2018) used as the reference catalog without proper motion corrections. The single-epoch astrometric accuracy is found to have a minimal value of ≈20 mas for DECam data taken close to the Gaia 2015.5 epoch; however, it is found to increase before and after that date (T. M. C. Abbott et al. 2021).

To remove image artifacts, we mask the saturated pixels caused by bright stars, and the associated charge overflow in both the readout direction ("bleed trails") and the CCD serial register ("edge bleeds"). We also perform cosmic-ray masking using a modified version of the algorithm developed for the Legacy Survey of Space and Time (LSST; M. Jurić et al. 2017) and a satellite streak mask using an algorithm based on the Hough transform (E. Morganson et al. 2018).

To account for the sky background light, we also fit and subtract the sky background from the whole DECam exposure using seasonally averaged principal component analysis components and divide the image by the star flat (G. M. Bernstein et al. 2017). The sky background model is produced from the raw bias, dome flat, and nightly star flat images and quantifies the differences between the dome flat and

the response to astronomical flux. The PSF for each CCD image is obtained using PSFEx (E. Bertin 2011). Finally, the source catalog for each individual CCD image is then produced using SourceExtractor (E. Bertin & S. Arnouts 1996) with a detection threshold of $\sim 3\sigma$ (T. M. C. Abbott et al. 2021).

The DELVE EDR3 coadded images were assembled from a subset of DECam exposures that were publicly available as of 2022 December 5. The coadd input exposures were selected to reside in the northern Galactic cap ($b > 10°$) and to have an exposure time between 30 and 350 s. Furthermore, we require that the images have a PSF FWHM value of between $0'' < \mathrm{FWHM} < 1\farcs55$ and that all exposures have an effective exposure timescale factor $t_{\mathrm{eff}} > 0.2$, where t_{eff} is calculated based on nominal values of the PSF FWHM, sky brightness, and transparency as described in E. Neilsen et al. (2016). We also require that the input exposures have a good astrometric solution when matched to Gaia DR2. This is achieved by requiring >250 astrometric matches, $\chi^2_{\mathrm{astrom}} < 180$, and an average difference of $\Delta_{\mathrm{astrom}} < 100$ mas. As with A. Drlica-Wagner et al. (2022), to remove exposures with excess electronic noise or poor sky background estimation resulting in many spurious object detections, we also require that the number of objects detected in each exposure is less than the empirically determined limit of 7.5×10^5. To improve the quality of the input exposures going into the coadding process, we further remove exposures that were identified as having suspect sky subtraction and/or astrometric fits based on selection criteria developed for DES (T. M. C. Abbott et al. 2021).

Since the public DECam exposures were taken for a wide variety of science purposes with different exposure times and filter distributions, there are variations in survey depth and filter coverage across the footprint. Therefore, to improve the uniformity of the data set, we select exposures to homogenize the cumulative effective exposure time across the DELVE footprint. This homogenization is performed by iteratively adding exposures to the coadd input list, starting with the exposure with the highest effective exposure time ($t_{\mathrm{eff}} \times t_{\mathrm{exp}}$). Exposures are iteratively added to the input list in order of effective exposure time unless >95% of the exposure area is already covered by 15 or more exposures in the same band. The homogenization process removed 11% of all the exposures and resulted in the standard deviation of the effective exposure time ($t_{\mathrm{eff}} \times t_{\mathrm{exp}}$) across the survey area in g band to drop from 1773 s to 630 s. This selection results in the selection of 61,425 exposures in the g, r, i, and z bands in the northern Galactic cap ($b > 10°$).

Individual CCD images are further checked for quality by automated algorithms and visual inspection (e.g., looking for issues similar to those described in P. Melchior et al. 2016). In particular, we identify images that are strongly affected by optical ghosting (S. M. Kent 2013), electronic noise variations, telescope motion (e.g., bad tracking, earthquakes, etc.), airplanes in the field of view, and other similar issues that lead to poor data quality. These quality checks are performed at both the exposure and individual CCD level, and the individual CCD images that contain artifacts are removed from the coadd input list. In total, 10,796 out of 6,440,109 CCD images were removed by this inspection.

Photometric calibration was performed by matching to the ATLAS RefCat2 reference catalog (J. L. Tonry et al. 2018). ATLAS RefCat2 is an all-sky catalog that combines several surveys (i.e., Gaia, PS1, SkyMapper, etc.). For the purposes of DELVE calibration, we utilize the PS1 measurements in the north (decl. $> -30°$) and SkyMapper measurements in the south (decl. $< -30°$). The calibration followed the procedure described for DELVE DR2 (A. Drlica-Wagner et al. 2022), but with an updated transformation procedure that finds the offsets required to convert the magnitudes for sources in different color bins and makes an interpolation for the intermediate color values (S. S. Allam & D. L. Tucker et al. 2024, in preparation).[29] Separate interpolations were derived for the northern (PS1) and southern (SkyMapper) parts of the sky by matching the DES DR2 WAVG_MAG_PSF magnitudes to the corresponding ATLAS RefCat2 magnitudes to remove the ~5 mmag offset detected in DELVE DR2 (A. Drlica-Wagner et al. 2022). Photometric zero-points for each DECam CCD were obtained by performing a $1''$ match between the DECam Final Cut catalogs and ATLAS RefCat2. The ATLAS RefCat2 measurements are transformed into the DECam system using interpolations, and the zero-point is derived from the median offset required to match the ATLAS RefCat2 values. We repeated the calibration process for each CCD three times, with each iteration removing outlier sources where the magnitude difference between the zero-point-calibrated sources and ATLAS RefCat2 values is $>3\sigma$ from the mean. The relative photometric uncertainty was validated through comparison to Gaia EDR3 using transformation equations derived for DES DR2 (T. M. C. Abbott et al. 2021) and by measurements of the width of the stellar locus following the procedures described in A. Drlica-Wagner et al. (2022). Calibrated single-epoch sources were found to agree with Gaia magnitudes with a scatter of ± 4.2 mmag (estimated using half the width of the 68% containment).

The image coaddition process follows that described in Section 6 of E. Morganson et al. (2018). Coadded images are built in distinct rectangular tiles that have dimensions of $0\fdg71 \times 0\fdg71$ covered by 10,000 pixels with a pixel scale of $0\farcs263$. Coadd images were constructed for tiles that had at least partial coverage in all four bands (g, r, i, and z). To minimize the FWHM of the coadded PSF due to astrometric offsets between input exposures, we recompute a global astrometric solution for all CCD images provided as input to each coadd tile. For each tile, we use SCAMP (E. Bertin 2006) to perform an astrometric refinement by simultaneously solving for the astrometry using the Final Cut catalogs for each input CCD and Gaia DR2 as an external reference catalog. Using this process, the DES pipeline obtained residuals from the simultaneous astrometric fit with a standard deviation of ~27 mas (T. M. C. Abbott et al. 2021). We then use SWARP (E. Bertin et al. 2002) to resample the input images and produce the final coadd images for all four bands (g, r, i, and z). In addition to the individual bands, we also produce a detection image, which is a coadd of the $r+i+z$ images using the COMBINE_TYPE = AVERAGE procedure in SWARP (T. M. C. Abbott et al. 2021).

Object detection is performed on the $r+i+z$ detection coadd image using SourceExtractor following the procedure described for DES DR2 (T. M. C. Abbott et al. 2021). Objects are detected when contiguous groups of four or more pixels exceed a threshold of 1.5σ, which has been found to correspond to a source detection threshold of $\sim 5\sigma$ (T. M. C. Abbott et al. 2021). Initial photometric measurement

[29] https://github.com/DouglasLeeTucker/TransformEqns

is performed with SourceExtractor in "dual image mode," using the detection image and the band of interest. Object astrometry comes from the windowed positions derived by SourceExtractor on the coadd images. The DELVE EDR3 footprint contains 6895 coadd tiles, which covers 7737 deg^2 with median limiting magnitudes of $g \sim 24.1$, $r \sim 23.6$, $i \sim 23.2$, and $z \sim 22.5$ (estimated at a signal-to-noise ratio (S/N) = 10 in 2″ aperture from survey property maps derived from the single-epoch images that go into the coadds). For comparison, the median limiting magnitudes of DES DR2 assessed at the same S/N with the same technique are $g \sim 24.7$, $r \sim 24.4$, $i \sim 23.8$, and $z \sim 23.1$ (T. M. C. Abbott et al. 2021). In contrast, the DELVE DR2 limiting PSF magnitudes at S/N = 10 are $g \sim 23.5$, $r \sim 23.1$, $i \sim 22.7$, and $z \sim 22.1$ (A. Drlica-Wagner et al. 2022).

We perform multiepoch photometric fitting following the procedures developed for cosmology analyses using the DES Year 3 DEEP fields (e.g., S. Everett et al. 2022; W. G. Hartley et al. 2022). We first create multiepoch data structures (MEDSs; M. Jarvis et al. 2016; J. Zuntz et al. 2018) consisting of cutouts centered on each object detected in the coadd images. The dimensions of the MEDSs range in size from 32×32 to 256×256 pixels, and they are comprised of the individual constituent images that went into the coadd at the location of each detected object. We perform multiband, multiepoch fitting using the fitvd tool (W. G. Hartley et al. 2022), which is built on top of the core functionality of ngmix (E. S. Sheldon 2014). We perform PSF model fits and bulge + disk model fits (BDF) while masking neighboring sources (i.e., a "single-object fit," in the DES nomenclature). The PSF model fits are obtained by fitting the amplitude of the individual-epoch PSF models, while the BDF fits consist of fitting a galaxy model with bulge and disk components that are Sérsic profiles with fixed indices of $n = 4$ and $n = 1$, respectively. To reduce the degeneracies in the parameters, the relative effective radii of the bulge and disk components in the BDF fits are fixed to unity. The magnitudes referenced in this paper are from the fitvd PSF fit, which has been found to provide the best photometry for point-like sources (T. M. C. Abbott et al. 2021).

We append several "value added" columns to the catalogs. Due to the increased depth of the DELVE EDR3 catalog relative to DELVE DR2 and the rapidly rising number density of faint background galaxies, the effects of star–galaxy misclassification can become more prominent in searches for resolved stellar systems. We perform star–galaxy separation using the sizes and S/Ns of the sources measured by the multiepoch fitvd fit following a classification procedure developed for DES Year 6 (K. Bechtol et al. 2024, in preparation). The classifier assigns an integer object class (ranging from 0 being likely stars to 4 being likely galaxies) to each source. Using DES data, a relatively pure sample of stars with $0 \leqslant$ EXT_FITVD $\leqslant 1$ has been found to have a stellar efficiency (true positive rate) of 90% with galaxy contamination (false discovery rate) of 10% when integrating over the magnitude range $19 \leqslant i \leqslant 23.5$, while a more complete stellar sample selected with $0 \leqslant$ EXT_FITVD $\leqslant 3$ has a stellar efficiency of 96% with galaxy contamination of 27% over the same magnitude range. The relative stellar efficiency (and galaxy contamination) of the classification procedure starts to drop (increase) strongly with magnitude starting at $i \sim 23$.

To calculate the extinction due to interstellar dust, we first obtain the value of $E(B-V)$ by performing a bilinear interpolation to the D. J. Schlegel et al. (1998) maps at the location of each source in the catalog. The reddening correction for each band is then calculated using the fiducial interstellar extinction coefficients from DES DR2 such that $A_b = R_b \times E(B-V)$ where $R_g = 3.186$, $R_r = 2.140$, $R_i = 1.569$, and $R_z = 1.196$ (T. M. C. Abbott et al. 2021). As described in T. M. C. Abbott et al. (2021), these coefficients include a renormalization of the $E(B-V)$ extinction values ($N = 0.78$) as suggested by E. F. Schlafly et al. (2010) and E. F. Schlafly & D. P. Finkbeiner (2011) so that they can be used directly with the $E(B-V)$ values from the D. J. Schlegel et al. (1998) map. In this paper, we denote extinction-corrected magnitudes with the subscript "0."

3. The Discovery of Leo VI

We search for resolved stellar systems in the DELVE EDR3 catalog using the simple matched-filter search algorithm (K. Bechtol et al. 2015; A. Drlica-Wagner et al. 2020).[30] This algorithm has been successfully used to discover more than 20 MW satellites to date (e.g., K. Bechtol et al. 2015; A. Drlica-Wagner et al. 2015; S. Mau et al. 2020; W. Cerny et al. 2021a, 2023b). To parallelize the search across the DELVE EDR3 footprint, we first partition the catalog into HEALPix at the scale of NSIDE = 32 (≈3.4 deg^2 pixel^{-1}). We then perform the search for each HEALPixelized catalog by combining the central catalog with catalogs from the eight neighboring HEALPixels.

In our simple satellite search, we select stars as sources with an object class of $0 \leqslant$ EXT_FITVD $\leqslant 1$. To reduce the effect of foreground contaminant stars, we only select stars that are consistent with an old ($\tau = 12$ Gyr), metal-poor ($Z = 0.0001$, [Fe/H] ~ -2.2) PARSEC isochrone (A. Bressan et al. 2012; Y. Chen et al. 2014, 2015; J. Tang et al. 2014). This is done by selecting stars that satisfy the following conditions $\Delta(g-r)_0 < \sqrt{0.10^2 + \sigma_g^2 + \sigma_r^2}$, where σ_g and σ_r are, respectively, the uncertainties of the g and r magnitudes of the individual stars. We perform the search multiple times as we scan the distance modulus of the isochrone in a range of $16.0 \leqslant m - M \leqslant 24.0$ mag at intervals of 0.5 mag. After the selection cuts, we smoothed the filtered stellar density field with a 1′ Gaussian kernel. We then identify overdensities in the stellar density field by iteratively increasing the density threshold until only 10 peaks remain. We computed the Poisson significance of the overdensities relative to the background stellar density (calculated using stars within a distance between 0.°3 and 0.°5 from the overdensity). We repeat the same procedure with the g- and i-band pair and select candidates with detection significance above a significance threshold of 5.5σ in both the g and r bands and g and i bands (similar to in W. Cerny et al. 2023b). For each dwarf galaxy candidate, we produce a diagnostic plot containing the smoothed stellar density and color–magnitude diagram (CMD) of the candidate, similar to Figure 1.

From the diagnostic plots, we identified a promising candidate stellar system near $(\alpha_{J2000}, \delta_{J2000}) = (171.°05, 24.°87)$ at a simple detection significance of 7.0σ in the g and r bands and 7.1σ in the g and i bands. Our analysis using follow-up observations of the system suggest it to be a newly

[30] https://github.com/DarkEnergySurvey/simple

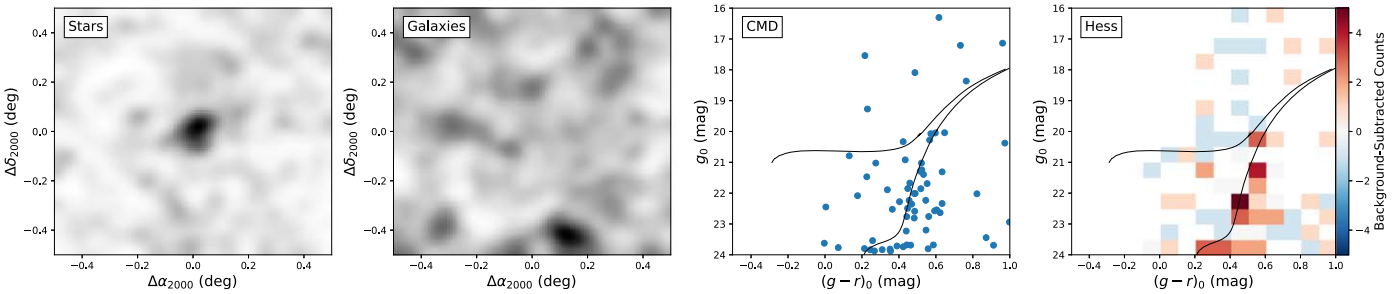

Figure 1. Diagnostic plots for Leo VI constructed with the deeper follow-up DECam photometric data. Left: smoothed isochrone-filtered spatial density of stars in the region around the Leo VI. The system appears as a significant overdensity against a relatively constant background. Center left: smoothed isochrone-filtered spatial density of galaxies. Center right: CMD of stars that are within $4'$ of the centroid of the system. Right: color–magnitude Hess diagram of the foreground stars within $4'$ of the centroid of Leo VI minus the background stars in a concentric annulus with radius from $12'$ to $12.'65$. We use the Ultrafaint GAlaxy LIkelihood (`ugali`) best-fit old ($\tau \sim 13.3$ Gyr), metal-poor ($Z = 0.0001$, [Fe/H] ~ -2.2) `PARSEC` isochrone with a distance modulus of $(m - M)_0 = 20.2$ for this figure.

discovered MW satellite UFD (see Section 7). Therefore, following historical convention, we refer to this system as Leo VI.[31]

Due to the lack of spatial coverage around Leo VI and the relatively shallow depth of the DELVE EDR3 data in this region, we obtained additional follow-up DECam imaging of the candidate so that more accurate morphological fits could be obtained. The follow-up observations consist of 3×300 s imaging in g and i band taken on 2023 June 17. To increase the depth of the follow-up imaging, we coadd the new exposures with archival DECam exposures around the candidate using the same pipeline as the DELVE EDR3 catalog. However, we have reduced the $t_{\rm eff}$ cut from $t_{\rm eff} > 0.2$ to $t_{\rm eff} > 0.15$ to include the new follow-up exposures that were taken during less than ideal observing conditions. Nevertheless, the looser $t_{\rm eff}$ cut still excludes one of the 300 s i-band follow-up exposures due to its low effective exposure timescale factor, $t_{\rm eff} \approx 0.07$, caused by cloudy and bright observing conditions.

Compared to the initial DELVE EDR3 data, the new imaging has an increased the depth by 0.3 mag in the g band and 0.4 mag in the i band, leading the `simple` detection significance to increase to 9.8σ in the g and r bands and 9.7σ in the g and i bands.

4. Morphological Fits

To obtain an estimate of the morphological properties of Leo VI and its stellar population, we use the maximum-likelihood-based `ugali` toolkit (K. Bechtol et al. 2015; A. Drlica-Wagner et al. 2020) on the follow-up DECam observations of the system. We model the stellar density profile of the system with an elliptical Plummer profile (H. C. Plummer 1911), with the free parameters described by the centroid coordinates ($\alpha_{\rm J2000}$, $\delta_{\rm J2000}$), angular semimajor axis length, $a_{\rm h}$, ellipticity, ϵ, and the position angle (PA) of the major axis (defined east of north). We then model the magnitudes and colors of the possible member stars with a `PARSEC` isochrone model (A. Bressan et al. 2012; Y. Chen et al. 2014, 2015; J. Tang et al. 2014) with free parameters being the distance modulus, $(m - M)_0$, age, τ, and the metallicity, $Z_{\rm phot}$, of the system. We also fit another free parameter: stellar richness, λ, which normalizes the total number of stars in the system (K. Bechtol et al. 2015; A. Drlica-Wagner et al. 2020).

We use the Markov Chain Monte Carlo sampler `emcee` (D. Foreman-Mackey et al. 2013) to simultaneously fit all the stellar density profiles and isochrone parameters in addition to the stellar richness (posterior distributions are shown in Figure A1). For star–galaxy separation, we loosen the stellar classification in our `ugali` analysis by defining stars to be sources with an object class of $0 \leqslant$ `EXT_FITVD` $\leqslant 3$ to include as many possible Leo VI member stars as possible in our analysis.

Table 1 shows the values and uncertainties of the stellar density profile and isochrone parameters obtained from `ugali`. The estimates of parameters are obtained from the median of the marginalized posteriors, while the 1σ uncertainties are obtained using the 16th and 84th percentiles. We find that posterior distribution for both the age of the system and the metallicity of the system peaked near $\tau = 13.5$ Gyr and $Z_{\rm phot} = 0.0001$ and [Fe/H] ~ -2.2, which represents oldest and most metal-poor isochrone in the A. Bressan et al. (2012) library. We discuss spectroscopic measurements of the metallicity in Section 5.3.

Table 1 also shows Leo VI properties derived from the fitted parameters. For example, we can obtain the azimuthally averaged angular half-light radius (defined as $R_{\rm h} = a_h\sqrt{1-\epsilon}$), the equivalent physical semimajor axis length (in parsecs), $a_{1/2}$, and azimuthally averaged physical half-light radius (in parsecs), $R_{1/2}$. Using the prescription defined N. F. Martin et al. (2008), we obtain the absolute V-band magnitude, M_V, from the isochrone and use it to derive the V-band luminosities (L_V). We also derive the stellar mass (M_*) of the system by assuming a stellar mass-to-light ratio of $M_*/L_V = 2$.

To investigate the robustness of the fits, we rerun `ugali` with different magnitude limit masks ranging from $g < 22.5$ to $g < 24.5$ mag at intervals 0.5 mag. We find that the fit results for all fitted parameters are consistent within 1σ with the uncertainty being generally smaller when using the deeper mask.

For each star, the `ugali` pipeline assigns a probability that the star is a member of the dwarf galaxy based on its spatial position, photometric properties, and local imaging depth assuming a given model that includes a putative dwarf galaxy and the local stellar field population (K. Bechtol et al. 2015; A. Drlica-Wagner et al. 2020). We plot the spatial distribution of stars in a small region around Leo VI, with stars colored by their `ugali` membership probability in the left plot of Figure 2. While in the right plot of same figure, we show a CMD of the system with its stars colored by their `ugali` membership probability and also show the best-fit `PARSEC`

[31] After Leo I, Leo II (R. G. Harrington & A. G. Wilson 1950), Leo A (Leo III; F. Zwicky 1942), Leo IV (V. Belokurov et al. 2007), and Leo V (V. Belokurov et al. 2008).

Table 1
Measured and Derived Parameters of Leo VI

Parameter	Description	Value	Units
Morphological Fits (Section 4)			
α_{J2000}	R.A. of centroid	$171.077^{+0.016}_{-0.013}$	deg
δ_{J2000}	Decl. of centroid	$24.874^{+0.008}_{-0.011}$	deg
a_h	Angular semimajor axis length	$4.17^{+1.14}_{-1.33}$	arcmin
$a_{1/2}$	Physical semimajor axis length	140^{+40}_{-40}	pc
R_h	Azimuthally averaged angular half-light radius	$2.84^{+0.78}_{-0.9}$	arcmin
$R_{1/2}$	Azimuthally averaged physical half-light radius	90^{+30}_{-30}	pc
ϵ	Ellipticity	$0.54^{+0.19}_{-0.29}$	…
PA	PA of major axis (east of north)	63^{+13}_{-20}	deg
$(m-M)_0$	Distance modulus[a]	$20.23^{+0.17}_{-0.12}$	mag
$D_\odot$	Heliocentric distance[a]	111^{+9}_{-6}	kpc
τ	Age[b]	>12.37	Gyr
M_V	Absolute (Integrated) V-band magnitude	$-3.56^{+0.47}_{-0.37}$	mag
L_V	V-band luminosity	2300^{+1200}_{-700}	$L_\odot$
M_*	Stellar mass (assuming $M_*/L_V = 2$)	4600^{+2300}_{-1400}	$M_\odot$
Stellar Kinematics and Metallicities (Section 5)			
N_{spec}	Number of spectroscopically confirmed members stars	9	…
v_{hel}	Heliocentric radial velocity	$170.03^{+1.75}_{-1.41}$	km s^{-1}
σ_v	Line-of-sight velocity dispersion	$2.85^{+1.57}_{-1.31}$	km s^{-1}
$M_{1/2}$	Dynamical mass within half-light radius[c]	$0.7^{+1.2}_{-0.5} \times 10^6$	$M_\odot$
$M_{1/2}/L_{V,1/2}$	Mass-to-light ratio within half-light radius[c]	700^{+1400}_{-500}	$M_\odot/L_\odot$
$[Fe/H]_{spec}$	Mean spectroscopic metallicity	$-2.39^{+0.10}_{-0.13}$	dex
$\sigma_{[Fe/H]}$	Metallicity dispersion	$0.19^{+0.14}_{-0.11}$	dex
Proper Motion, Orbits, and J-factor (Section 6)			
$\mu_{\alpha*}$	Proper motion R.A.	$-0.06^{+0.18}_{-0.20}$	mas yr^{-1}
μ_δ	Proper motion decl.	$-0.22^{+0.22}_{-0.17}$	mas yr^{-1}
d_{GC}	Galactocentric distance	114^{+7}_{-7}	kpc
r_{apo}	Orbital apocenter	162^{+109}_{-11}	kpc
r_{peri}	Orbital pericenter	103^{+11}_{-53}	kpc
e	Orbital eccentricity	$0.58^{+0.12}_{-0.03}$	…
$\log_{10} J(0.^\circ5)$	J-factor within a solid angle of $0.^\circ5$	$17.3^{+0.9}_{-1.0}$	GeV^2 cm^{-5}

Notes. Details of each parameter can be found in their corresponding sections.
[a] Following A. Drlica-Wagner et al. (2015), we added in quadrature a 0.1 mag systematic uncertainty to the distance modulus measurement to account for the uncertainties in the isochrone modeling.
[b] The posterior distribution peaked near $\tau = 13.5$ Gyr corresponding to our oldest available PARSEC isochrone, we therefore quote the 68% Bayesian lower limit.
[c] Based on single-epoch velocities and assuming dynamical equilibrium.

isochrone model (A. Bressan et al. 2012; Y. Chen et al. 2014, 2015; J. Tang et al. 2014).

Being excellent standard candles (M. Catelan & H. A. Smith 2015), the presence of RR Lyrae (RRL) stars in Leo VI could be used to obtain an independent and more accurate distance estimate of the system (C. E. Martínez-Vázquez et al. 2019). We search the Gaia DR3 (G. Clementini et al. 2023) and PS1 RRL (B. Sesar et al. 2018) catalogs for RRL stars around Leo VI, but find no RRL stars within $0.^\circ2$ of the centroid of Leo VI. This is expected as the location of the horizontal branch at $g \sim 21$ is around the magnitude limit of Gaia and thus deeper multiepoch observations are needed to detect potential RRL stars.

5. Stellar Kinematics and Metallicities

5.1. Keck Observations

To confirm that Leo VI is a physically bound stellar system and not a chance arrangement of MW stars, we took follow-up spectroscopic observations of the potential member stars with DEIMOS mounted on the Keck II telescope (S. M. Faber et al. 2003).

We obtained 1.0 hr of DEIMOS observations of Leo VI through on the night of 2024 February 14.[32] These observations used a single multiobject mask with slits of width $0.''7$ and a minimum length of $4.''5$. Targets were selected primarily based on the photometric probabilities provided by a `ugali` fit to the follow-up DECam imaging, as well as the astrometric information provided by Gaia. We used the DEIMOS 1200G grating and OG550 order blocking filter; this configuration provides $R \approx 6000$ across a wavelength range spanning Hα, the telluric A band, and the Ca II triplet (CaT) region ($\sim$6500–9000 Å). All exposures were reduced using the official Keck Data Reduction Pipeline found in the `PypeIt` software package (J. Prochaska et al. 2020), with `PypeIt`'s default flexure correction disabled. Wavelength calibration was

[32] Due to an earthquake-induced motor failure, the Keck II dome could not rotate during our run, limiting our total exposure time to when Leo VI transited the fixed azimuth window set by the dome slit. All of our exposures suffered from vignetting from the dome, resulting in lower S/N but no other consequences of note.

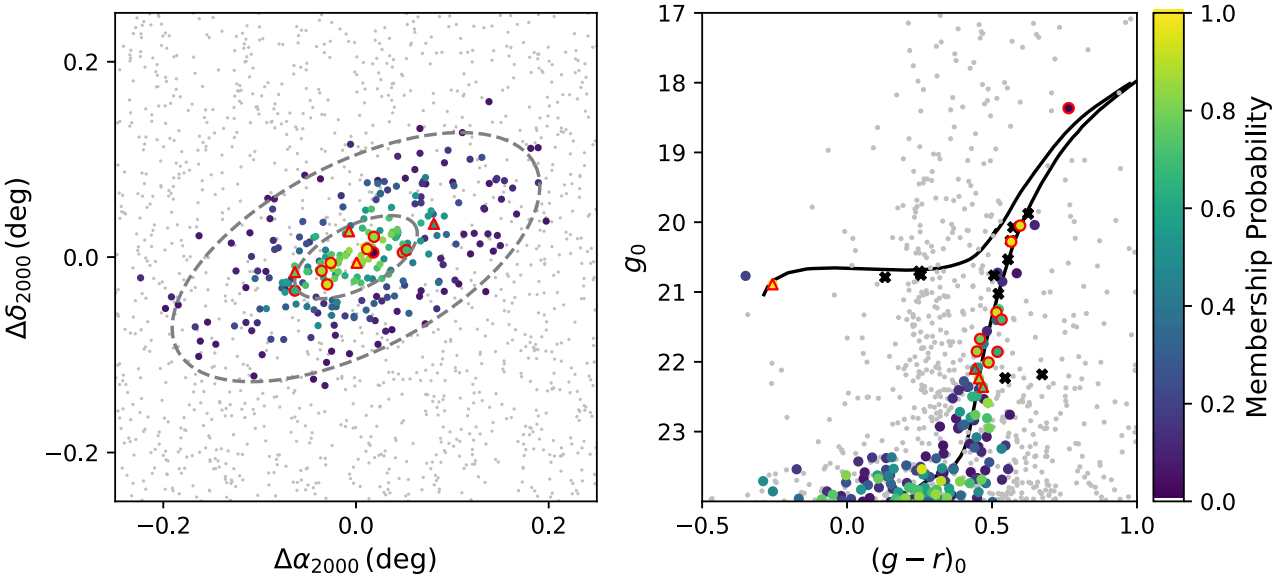

Figure 2. Left: map of likely member stars in the vicinity of the Leo VI system, with stars colored by their `ugali` membership probability. Stars with a lower `ugali` membership probability ($p < 0.05$) are shown in gray. Right: CMD of likely member stars in the system, again colored by their `ugali` membership probability. In both plots, stars with a red outline represent spectroscopically confirmed member stars (circles) and candidate member stars (triangles) of Leo VI (Section 5). The black crosses denotes sources that have confirmed to be nonmembers of Leo VI either through their inconsistent spectroscopic radial velocity, high Gaia proper motion, or Gaia classification as likely quasi-stellar objects. The black curve represents the `ugali` best-fit `PARSEC` isochrone ($\tau \sim 13.3$ Gyr, $Z = 0.0001$, and $(m - M)_0 = 20.2$).

performed using XeNeArKr arcs, and flat-fielding used internal quartz flats.

5.2. Line-of-sight Velocities and Stellar Membership

We obtain the line-of-sight velocities of the potential member stars using the `DMOST` package (M. Geha et al. 2024, in preparation), which is a dedicated measurement pipeline for spectra obtained from DEIMOS 1200G grating.[33] The `DMOST` package measures line-of-sight velocities by forward modeling the spectrum of a star using both a `PHOENIX` stellar atmosphere library template (T. O. Husser et al. 2013) and a `TelFit` telluric absorption spectrum template (K. Gullikson et al. 2014); the latter is used to correct for wavelength shifts induced by the mis-centering of stars within their slits. The final velocity uncertainty is calculated by adding in quadrature the scaled statistical uncertainty and a 1.1 km s^{-1} uncertainty floor. Further details about the velocity measurement procedure implemented within `DMOST` can be found in M. Geha et al. (2024, in preparation).

Starting from our initial target sample of 44 stars, we were able use the pipeline to obtain line-of-sight velocity measurements for 25 stars. We can see from the left subplot of Figure 3 an excess of 13 stars with a line-of-sight velocity, $v_{\rm hel}$, in the range of 155 km s^{-1} $\leqslant v_{\rm hel} \leqslant$ 185 km s^{-1}, which we infer to be possible member stars of Leo VI, thus confirming the nature of Leo VI as a gravitationally bound system. We find nine spectroscopically confirmed member stars with line-of-sight velocity measurements that are precise enough to be included in the systemic analysis ($\epsilon_{v_{\rm hel}} < 10$ km s^{-1}), and four additional candidate member stars with less precise velocity measurements. Table 2 shows the basic properties of the confirmed and candidate member stars. Based on their DECam photometry and the best-fit `ugali` isochrone for Leo VI (see Figure 2), we identify these 13 Leo VI member stars as 12 red giant branch (RGB) stars and one blue horizontal branch (BHB) star.

We obtain the systemic velocity, $v_{\rm hel}$, and velocity dispersion of the system, σ_v, from the line-of-sight velocity measurements of the nine confirmed member stars using a single two-parameter fit as described in M. G. Walker et al. (2006). For the model fit, we apply a uniform prior on the systemic velocity within a range of $164.6 < v_{\rm hel} < 178.6$ km s^{-1}, based on the maximum and minimum range of velocities found in the member stars, and a log-uniform prior on the velocity dispersion within a range of $-1 < \log_{10}(\sigma_v/{\rm km\ s^{-1}}) < 1$. Using `emcee` to obtain the marginalized posterior distribution (shown in Figure A2), we find that the systemic velocity of Leo VI is given by $v_{\rm hel} = 170.03^{+1.75}_{-1.41}$ km s^{-1}, while the velocity dispersion is given by $\sigma_v = 2.85^{+1.57}_{-1.31}$ km s^{-1}. We determine the values of the parameters and their uncertainties from the peak and the highest density region containing 68% of the posterior (R. J. Hyndman 1996). The middle subplot of Figure 3 shows the best-fit velocity dispersion model overlaid on a histogram of the measured radial velocity of the Leo VI stars. We find that the best-fit velocity dispersion remains consistent within the uncertainties if we instead assume a uniform prior from $0 < \sigma_v < 10$ km s^{-1} (Figure A2).

To further test the robustness of the systemic velocity and velocity dispersion measurements from outlier measurements, we performed a jackknife test where we recalculated the parameters for a subsample of stars where one star is removed from the total population at a time. As seen in Figure 4, we found that the velocity measurements are mostly dominated by the three highest S/N stars. If we remove either of the two very-high-S/N stars, Gaia DR3 3993822949622182272 ($v_{\rm hel} = 164.6 \pm 1.6$ km s^{-1}) or Gaia DR3 3993823052701408128 ($v_{\rm hel} = 174.0 \pm 1.7$ km s^{-1}), which show a large difference in the line-of-sight velocity between each other, our velocity dispersion measurements become unresolved (i.e., consistent with a zero velocity dispersion measurement). For stars with S/N < 15, the values of parameters

[33] https://github.com/marlageha/dmost

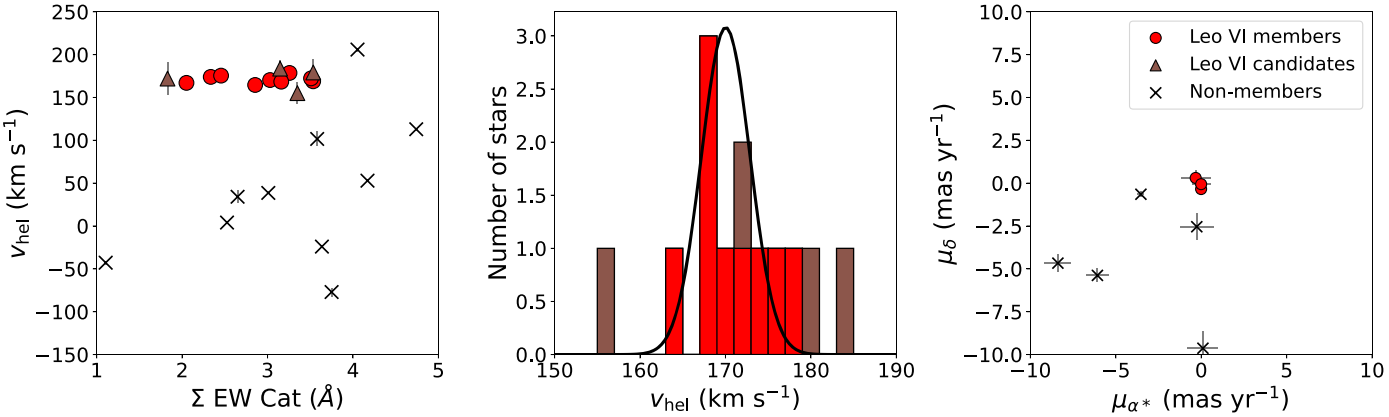

Figure 3. Left: the equivalent widths (EWs) of the CaT lines vs. the measured line-of-sight (radial) velocity of the target stars. The plot shows a prominent excess of stars around 155 km s^{-1} $\leqslant v_{hel} \leqslant$ 185 km s^{-1}, which we assumed to be member stars (red circles) and candidate member stars (brown triangles) of Leo VI. The gray bars show the uncertainties of the line-of-sight (radial) velocity measurement. Middle: histogram of the measured heliocentric radial velocity of the Leo VI member stars and candidate member stars overlaid with the best-fit velocity dispersion model (see Section 5.2). We note that the histograms does not capture the large uncertainties in the velocity measurements for the low-S/N stars. Right: proper motions of spectroscopic targets that are bright enough ($g \lesssim 21$) to be measured in Gaia DR3. Three of the spectroscopically confirmed member stars that also contain Gaia proper motion measurements (red circles) are found to be clustered near μ_δ, $\mu_\alpha \cos(\delta) \sim (0, 0)$ mas yr^{-1}.

Table 2
Properties of Spectroscopically Confirmed Member Stars and Candidate Member Stars of Leo VI Ordered by Decreasing Keck/DEIMOS Spectrum Signal-to-noise Ratio

Star Name	R.A. (deg)	Decl. (deg)	g_0 (mag)	r_0 (mag)	S/N	v_{hel} (km s^{-1})	Σ EW CaT (Å)	[Fe/H] (dex)	Type
Gaia DR3 3993822846542975360	171.096	24.878	18.4	17.6	66.6	168.9 ± 1.1	3.53 ± 0.21	−2.60 ± 0.10	RGB
Gaia DR3 3993822949622182272	171.048	24.868	20.1	19.4	22.0	164.6 ± 1.6	2.85 ± 0.28	−2.50 ± 0.13	RGB
Gaia DR3 3993823052701408128	171.090	24.882	20.3	19.7	18.9	174.0 ± 1.7	2.34 ± 0.37	−2.69 ± 0.16	RGB
Gaia DR3 3993822502945568128	171.044	24.846	21.3	20.8	7.7	170.3 ± 4.0	3.03 ± 0.37	−2.14 ± 0.17	RGB
Leo VI J112432.23+245250.95	171.134	24.881	21.4	20.9	7.7	172.3 ± 3.4	3.51 ± 0.44	−1.89 ± 0.19	RGB
Leo VI J112431.27+245242.21	171.130	24.878	21.7	21.2	5.8	175.5 ± 4.5	2.46 ± 0.53	−2.33 ± 0.23	RGB
Leo VI J112423.32+245340.09	171.097	24.894	21.9	21.4	4.8	178.6 ± 6.6	3.26 ± 0.77	−1.90 ± 0.34	RGB
Leo VI J112401.61+245021.90	171.007	24.839	21.9	21.3	3.9	168.4 ± 8.3	3.16 ± 0.59	−1.95 ± 0.26	RGB
Leo VI J112408.96+245134.74	171.037	24.860	22.0	21.5	3.7	167.0 ± 7.0	2.05 ± 0.65	−2.48 ± 0.30	RGB
Leo VI J112418.58+245204.63	171.077	24.868	20.9	21.1	4.3	179.2 ± 15.1	⋯	⋯	BHB
Leo VI J112439.81+245428.12	171.166	24.908	22.1	21.7	3.5	183.6 ± 10.3	⋯	⋯	RGB
Leo VI J112416.48+245400.62	171.069	24.900	22.2	21.8	3.4	172.0 ± 19.0	⋯	⋯	RGB
Leo VI J112401.62+245130.33	171.007	24.858	22.4	21.9	2.5	155.0 ± 12.7	⋯	⋯	RGB

Note. The top section lists confirmed member stars with line-of-sight velocity errors of $\epsilon_{v_{hel}} < 10$ km s^{-1}, while the bottom section contains candidate member stars with less precise velocity data ($\epsilon_{v_{hel}} > 10$ km s^{-1}). Details of each parameter can be found in Section 5.

obtained from the jackknife test are all within 1σ of the parameters obtained from the full sample. However, since we only have single-epoch radial velocity measurements, we cannot identify any of the Leo VI member stars as unresolved binary systems that can inflate the system's velocity dispersion. Some studies suggest the binary fraction of UFDs could be as high as 50% (Q. E. Minor et al. 2019; J. M. Arroyo-Polonio et al. 2023). Furthermore, some of the stars could also be nonmember interlopers.

If we assume that Leo VI is a dispersion-supported system in dynamical equilibrium, we can use the estimator from J. Wolf et al. (2010) with the velocity dispersion measurement of Leo VI to calculate its enclosed mass:

$$M_{1/2} = 930 M_\odot \left(\frac{\sigma_{v,los}}{\text{km s}^{-1}}\right)^2 \left(\frac{R_{1/2}}{\text{pc}}\right). \quad (1)$$

We estimate that the dynamical mass of the system within the half-light radius is $0.7^{+1.2}_{-0.5} \times 10^6$ $M_\odot$. Assuming that the luminosity at the half-light radius is given by $L_{1/2} = 0.5\ L_V$, we obtain that the mass-to-light ratio at the half-light radius of Leo VI is given by $700^{+1400}_{-500} M_\odot/L_\odot$.

However, the high ellipticity of Leo VI may indicate that the system might be tidally disturbed by the MW, which would make the assumption of dynamical equilibrium invalid. We will further discuss the possibility of Leo VI being a tidally disrupted system in Section 6.2.

5.3. Metallicity and Metallicity Dispersion

In addition to the line-of-sight velocities, DMOST also measures the equivalent widths (EWs) of the infrared CaT lines. In this analysis, we model the CaT lines of high-S/N stars (S/N > 15) with a combination of Gaussian and Lorentzian models, while we model the rest of the stars (S/N < 15) with a single Gaussian model. We note that our EW measurements are only valid for RGB stars, so we exclude the EW CaT measurement for the BHB star. We also excluded EW CaT measurements for RGB stars with high line-of-sight velocity errors ($\epsilon_{v_{hel}} > 10$ km s^{-1}).

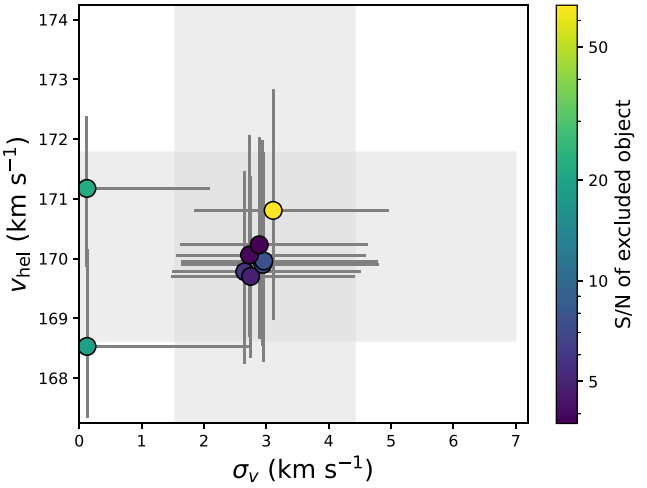

Figure 4. Jackknife test for the radial velocity parameters of Leo VI. The gray regions represent the 68% percentile uncertainty of the parameters obtained from the full sample. Each point represents the parameters obtained using a subsample that has excluded one star. The velocity dispersion measurement of the system becomes unresolved when we remove either one of the two very-high-S/N stars (S/N $>$ 15) with a large difference in line-of-sight velocity between each other ($v_{\rm hel}$ = 164.6 $\pm$ 1.6 and 174.0 $\pm$ 1.7 km s^{-1}).

We derived [Fe/H] metallicities from the EWs using the calibration relation from R. Carrera et al. (2013). The calibration relation requires the absolute V-band magnitude for each star, which we obtain using their g- and r-band magnitudes from the follow-up DECam catalog. We then convert the g and r magnitudes into relative V-band magnitude using transformation relations from T. M. C. Abbott et al. (2021) and subtract the relative magnitudes with distance modulus from the `ugali` fit (Table 1) to obtain the absolute V-band magnitudes.

We derive the systemic metallicity and metallicity dispersion of Leo VI using `emcee` with a similar two-parameter fit as described for the systemic velocity, using only metallicity measurements for the six member stars with S/N $>$ 5. We apply a uniform prior on the spectroscopic metallicity of the system within the range of $-4 < [{\rm Fe/H}]_{\rm spec} < 0$ and a log-uniform prior on the metallicity dispersion in the range $-1.5 < \log_{10}(\sigma_{\rm [Fe/H]}) < 0.5$. We find that the systemic spectroscopic metallicity of Leo VI is $[{\rm Fe/H}]_{\rm spec} = -2.39^{+0.10}_{-0.13}$ and has a metallicity dispersion of $\sigma_{\rm [Fe/H]} = 0.19^{+0.14}_{-0.11}$ (see Figure A3). Similar with the velocity dispersion measurement, we repeated the analysis with uniform priors on the metallicity dispersion within the range $0 < \sigma_{\rm [Fe/H]} < 3$ and find that the metallicity and metallicity dispersion are within 1σ of the original values (Figure A3).

As shown in Figure 5, we find the size–luminosity, luminosity–metallicity, and luminosity–velocity dispersion relations of Leo VI to be consistent with other MW satellite galaxies.

6. Discussion

There are several unique properties of Leo VI that make its discovery particularly interesting, namely its highly elliptical shape and proximity to other MW satellites. We first discuss the orbital properties of Leo VI derived by combining Keck radial velocity measurements with Gaia proper motion measurements in Section 6.1. We then discuss whether Leo VI's elliptical shape might indicate that it is undergoing tidal disruption in Section 6.2. In Section 6.3, we consider the possibility of Leo VI being part of a group infall scenario due to its proximity to other satellite galaxies in the constellations of Leo and Crater.

6.1. Proper Motion and Orbit of Leo VI

To obtain 3D velocity information of the system, we crossmatch our DECam-based stellar catalog with the Gaia DR3 (Gaia Collaboration et al. 2023). As shown in the right subplot of Figure 3, all three spectroscopically confirmed member stars of Leo VI which also have Gaia proper motion measurements have proper motions clustered near μ_δ, $\mu_\alpha \cos(\delta) \sim (0, 0)$ mas yr^{-1}, further confirming that it is a gravitationally bound system that is located far from the MW. Using `emcee` to fit a Gaussian mixture model and taking into account for the correlations in $\mu_{\alpha*}$ and μ_δ, we find that the systemic proper motion of Leo VI is $\mu_{\alpha*} = -0.06^{+0.18}_{-0.20}$ mas yr^{-1} and $\mu_\delta = -0.22^{+0.22}_{-0.17}$ mas yr^{-1}.

To determine the orbit of Leo VI, we integrated 1000 realizations of its orbit using the `gala` galactic dynamics package (A. M. Price-Whelan 2017). We obtain a sample of the possible current 6D positions and velocities ($\alpha_{\rm J2000}$, $\delta_{\rm J2000}$, $D_\odot$, $\mu_{\alpha*}$, μ_δ, and $v_{\rm hel}$) of the system by sampling from the Gaussian error distribution of the observed position and velocity parameters (see Table 1), and convert it to the `astropy` v4.0 Galactrocentric frame (Astropy Collaboration et al. 2013). We then rewind Leo VI's orbit back in time for 10 Gyr in the presence of `gala`'s `MilkyWayPotential` model (J. Bovy 2015) and recorded `gala`'s estimate of the orbital parameters of Leo VI. We find an orbital apocenter of 162^{+109}_{-11} kpc, while the pericenter is 103^{+11}_{-53} kpc and the orbital eccentricity is $0.58^{+0.12}_{-0.03}$. Following the velocity and metallicity dispersion analyses, we obtain the best-fit values and uncertainties of the parameters from the peak of the distribution and the highest density region containing 68% of the posterior, respectively. At a heliocentric distance of $D = 111^{+9}_{-6}$ kpc, a proper motion uncertainty of 0.2 mas yr^{-1} corresponds to a velocity uncertainty of $\sim$100 km s^{-1}, introducing large uncertainties into our orbit estimates.

Moreover, the z-component of the specific angular momentum, L_z, and the specific orbital energy of the system, E, are given by $L_z = -4.16 \pm 4.71$ kpc^2 Myr^{-1} and $E = -0.024 \pm 0.023$ kpc^2 Myr^{-2}, respectively. We further find that 79% of realizations of Leo VI's orbit is bounded ($E < 0$ kpc^2 Myr^{-2}) and 84% of the realizations yield a prograde orbit.

6.2. Possible Tidal Disruption

Due to the high ellipticity of Leo VI, coupled with the fact that the direction of systemic proper motion aligns with the semimajor axis (see left panel of Figure 7), we discuss the possibility of the system being tidally disturbed by the MW. Common dynamical mass estimators for UFDs (such as J. Wolf et al. 2010) are based on the assumption that the system is in dynamical equilibrium, which does not apply to disrupting systems. Therefore, determining whether the system is in dynamical equilibrium or has been tidally disturbed has important implications for measurements of its dark matter content.

To assess whether the system is experiencing tidal disruption, we follow the methodology of A. B. Pace et al.

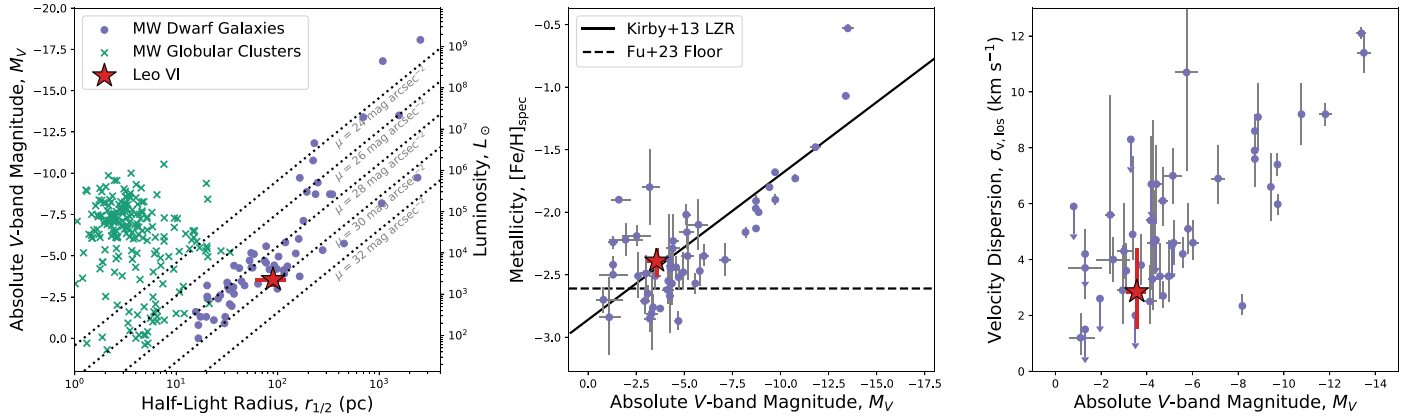

Figure 5. Left: the absolute V-band magnitude, M_V, vs. the azimuthally averaged physical half-light radius, $R_{1/2}$, of Leo VI and the population of known Local Group globular clusters and dwarf galaxies. Leo VI's morphological properties are consistent with those of a dwarf galaxy. Middle: the systemic metallicity, [Fe/H], vs. the absolute V-band magnitude of Leo VI and the population of Local Group dwarf galaxies. The overlaid black line represents the V-band absolute luminosity–metallicity relation ("LZR") found in E. N. Kirby et al. (2013), while the dashed black line represents the metallicity floor of [Fe/H] = −2.61 proposed for faint systems (S. W. Fu et al. 2023) Right: the line-of-sight velocity dispersion, $\sigma_{v,los}$, vs. absolute V-band magnitude of the population of Local Group dwarf galaxies.

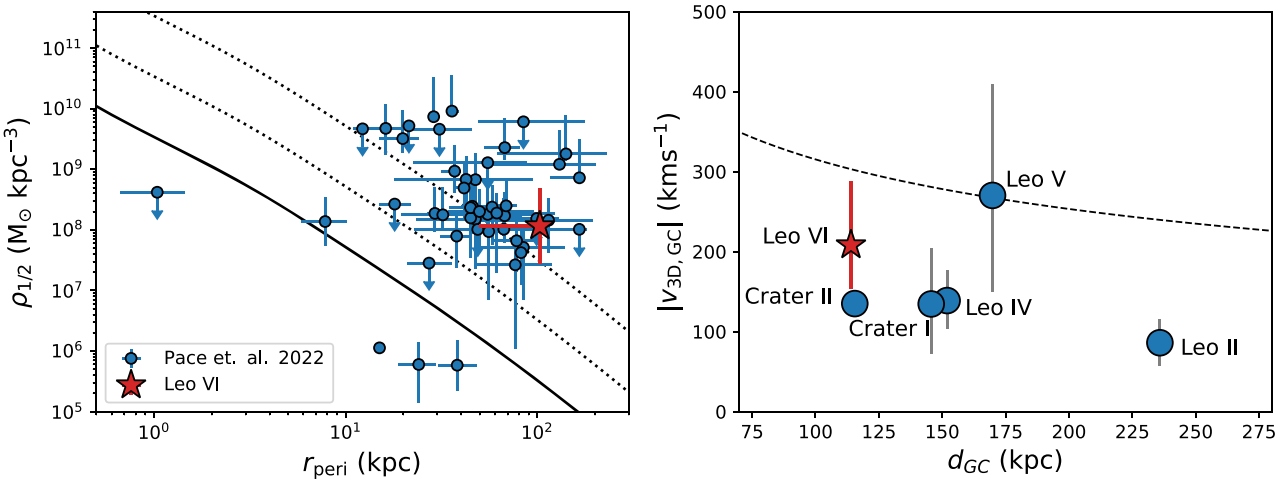

Figure 6. Left: the average density within the half-light radius, $\rho_{1/2}$, vs. distance of the pericenter, r_{peri}, of Leo VI and other MW satellites (A. B. Pace et al. 2022). The solid black line represents twice the enclosed MW density as a function of radius, while the dashed lines represent 20 and 200 times the enclosed MW density. If a satellite is located below the solid line, its half-light radius is estimated to be bigger than its Jacobi (tidal) radius and it is likely to be tidally disrupting (A. B. Pace et al. 2022). Right: the magnitude of the 3D Galactocentric velocity, $|V_{3D,GC}|$, vs. the Galactocentric distance, d_{GC}, of Leo VI and other nearby satellite galaxies. The dashed lines represented the escape velocity of the potentials from `gala`'s `MilkyWayPotential` potential. Leo VI is likely a bound system, and thus it is likely to have reached its orbital pericenter at least once in the past.

(2022) and compare the average density of Leo VI within its half-light radius, $\rho_{1/2} = 1.2^{+3.8}_{-0.9} \times 10^8 M_\odot$ kpc^{-3}, to twice the average MW density at its orbital pericenter $2\rho_{MW}(r = r_{peri}) = 6.6^{+38.8}_{-3.6} \times 10^5 M_\odot$ kpc^{-3}. If we assume a flat rotation curve for the MW and that Leo VI has an circular orbit, this comparison is equivalent to comparing the half-light radius of the system with its Jacobi (or tidal) radius where beyond it the tidal forces exceed the systems own gravitational force. As illustrated in Figure 6, the average density Leo VI is much higher than twice the average MW density. Therefore, Leo VI's Jacobi radius is likely larger than its half-light radius even when it is at its orbital pericenter, and that it is unlikely that the system is tidally disrupting. This conclusion also holds even when using the 1σ lower bounds for both the average density of Leo VI and its pericenter distance. However, we note that this approximation does not hold for all systems as the FIRE simulation has found the presences of high-density satellites galaxies which are still tidally disrupting (N. Shipp et al. 2023). In addition, Figure 6 shows the measured 3D velocity of Leo VI with other nearby satellites compared to the local escape velocity of `gala`'s `MilkyWayPotential` potential. It is likely that Leo VI is a bound system and that it is not on first infall, allowing the possibility of the system to reach its pericenter (at 103^{+11}_{-53} kpc) in the past.

Another signature of a tidally disrupting system is the presence of a velocity gradient in its member stars. Figure 7 illustrates the radial velocity of the spectroscopically confirmed member stars of Leo VI as a function of on-sky position and distance along the semimajor axis. To measure the velocity gradient of the system, we use a linear model to fit the radial velocity of the nine Leo VI members stars as a function of distance along the semimajor axis while taking account of intrinsic scatter. Using `emcee` to sample the posterior of the linear model, we find a large best-fit velocity gradient with large uncertainties, 78^{+48}_{-49} km s^{-1} deg^{-1} (40^{+25}_{-25} km s^{-1} kpc^{-1}). When performing a Bayesian information criterion test, we find that the nonzero velocity gradient model is mildly preferred over the zero velocity gradient model at $\Delta_{BIC,01} = 1.3$. However, we note that as

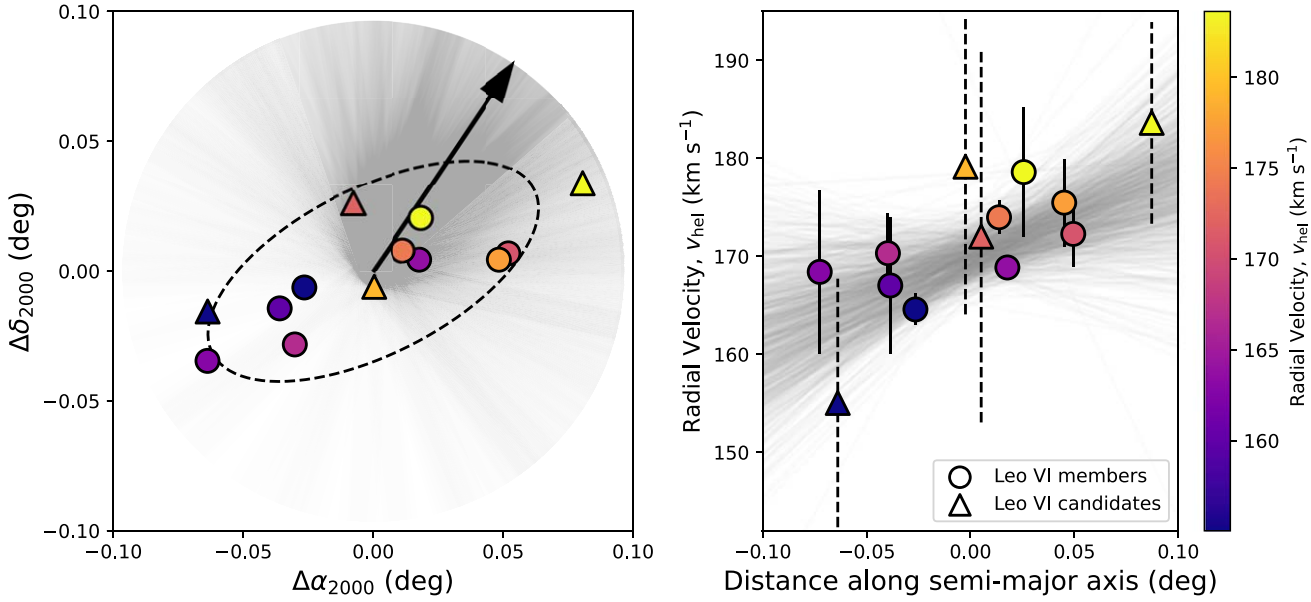

Figure 7. Left: spatial distribution of the spectroscopically confirmed Leo VI member stars (circles) and candidate member stars (triangles) with points colored by the measured line-of-sight (radial) velocity. The dashed ellipse shows the half-light radius of Leo VI. The direction of the median systemic proper motion (after correcting for solar reflex motion), computed from the three spectroscopically confirmed members with Gaia proper motion measurements, are shown with the black arrow, while the faint gray lines represent the 1000 Monte Carlo samplings from the proper motion uncertainties. The direction of proper motion aligns with the semimajor axis of Leo VI. Right: the line-of-sight (radial) velocity of Leo VI member stars (circles) and candidate member stars (triangles with dashed error bars) as a function of distance along its semimajor axis. The gray lines represent the Monte Carlo samplings used to measure the radial velocity gradient of the system along the semimajor axis. Due to the low number statistics and high uncertainty of the radial velocity measurements, we are unable to conclusively determine the presence/absence of a velocity gradient.

with the velocity dispersion analysis, the velocity gradient analysis is dominated by the three highest S/N stars, and that removing any of these stars from the sample has a large impact on the velocity gradient. For example, if we remove the member star Gaia DR3 3993822949622182272 from our sample, the velocity gradient drops to 47^{+56}_{-54} km s^{-1} deg^{-1} (24^{+29}_{-28} km s^{-1} kpc^{-1}). Therefore, we caution that the apparent velocity gradient might be a product of small number statistics and that more measurements are needed.

Moreover, both observations of MW satellites (A. B. Pace et al. 2022) and *N*-body simulations (R. R. Muñoz et al. 2008) have found no strong correlation between the ellipticity of a system and whether it is tidal disrupting. A. B. Pace et al. (2022) also observed that the proper motion vector of highly elliptical UFDs often aligns with the semimajor axis even for nondisrupting systems with large pericenters.

6.3. Group Infall Scenario

The on-sky location of Leo VI is close to several other known distant MW satellite galaxies that are already found in the constellations Leo and Leo Minor. Due to their similar on-sky positions and radial velocity, it has been suggested that the MW satellite galaxies in Leo (Leo II, Leo IV, and Leo V), the star cluster Crater/Laevens 1, and the dwarf galaxy Crater II might have been accreted into the MW through a group infall scenario (G. Torrealba et al. 2016; M. S. Pawlowski 2021; M. P. Júlio et al. 2024). Moreover, simulations from Y.-S. Li & A. Helmi (2008) have shown that about one-third of subhaloes are accreted onto the MW through infall groups. In this section, we discuss the possibility of Leo VI and other close-by systems such Leo Minor I (W. Cerny et al. 2023b), Hydra II (N. F. Martin et al. 2015), and Centaurus I (S. Mau et al. 2020) being members of the proposed Crater-Leo infall group.

G. Torrealba et al. (2016) found that the member systems of the Crater-Leo infall group are all located close to the great circle with the pole at (α, δ) = (83.°2, −11.°8) and form a consistent heliocentric distance gradient as a function of their decl. Figure 8 shows the heliocentric distance of Leo VI and the other members of the infall group as a function of their spatial distribution. From the figure, we can see that both Leo VI and especially Leo Minor I are too close to follow the heliocentric distance gradient exhibited by the other members of the infall group. While the distances of Hydra II and Centaurus I are more consistent with the other members of the group, their distances are not consistent with the distance trend from G. Torrealba et al. (2016).

We expect that satellites that are accreted into the MW via an infall group to share similar values of total energy and angular momentum (D. Lynden-Bell & R. M. Lynden-Bell 1995). Using `gala`'s `MilkyWayPotential` model and the velocity measurements of the Crater-Leo group collected from M. P. Júlio et al. (2024), we calculated the specific angular momentum and specific energy distribution of the member satellites of the Crater-Leo group. For Hydra II and Centaurus I, we use proper motion and radial velocity measurements from E. N. Kirby et al. (2015), A. B. Pace et al. (2022), and M. E. Heiger et al. (2024). We exclude Leo Minor I from the following analysis due to the lack of radial velocity measurements. As shown in Figure 9, the distribution of specific energy, E, and the square of the specific angular momentum squared, L^2, of four satellites (Leo II, Leo IV, Leo V, and Crater) all intersect each other at (L^2, E) ∼ (780 kpc^4 Myr^{-2}, −0.023 kpc^2 Myr^{-2}) suggesting a common origin (M. S. Pawlowski 2021). We find that the

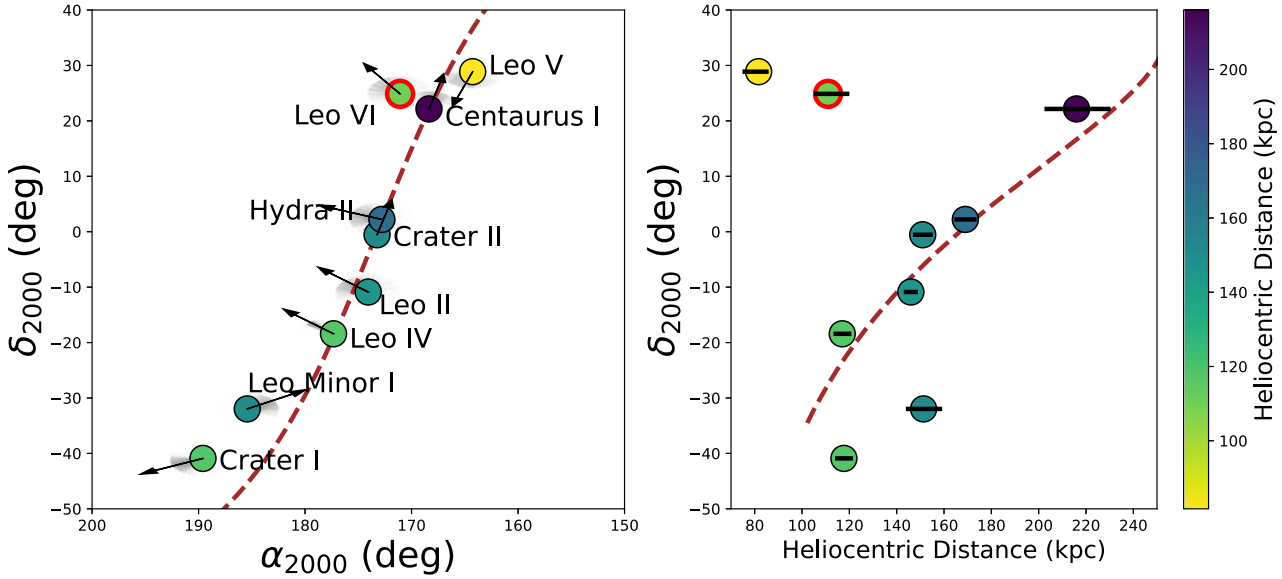

Figure 8. Left: spatial distribution of Leo VI and other potential members of the Crater-Leo infall group. The markers are colored based on the heliocentric distance of the system. The black arrows represent the direction of the median systemic proper motion of the system (after correcting for solar reflex motion), while the faint gray lines represent the 1000 Monte Carlo samplings from the proper motion uncertainties. The proper motion for the members of the Crater-Leo infall group were obtained from M. P. Júlio et al. (2024), where we have use their Hubble Space Telescope measurements for Leo IV and Leo V. The brown line represents a great circle with a pole centered at (83°.2, −11°.8) that passes close to the members of the infall group (G. Torrealba et al. 2016). Right: the heliocentric distance of Leo VI and the nearby satellites as a function of decl., δ_{J2000}. The brown line shows the orbit of the proposed Crater-Leo group from G. Torrealba et al. (2016). The plots indicate that the heliocentric distances of Leo VI and Leo Minor I are inconsistent with the distance gradient followed by the members of the Crater-Leo group.

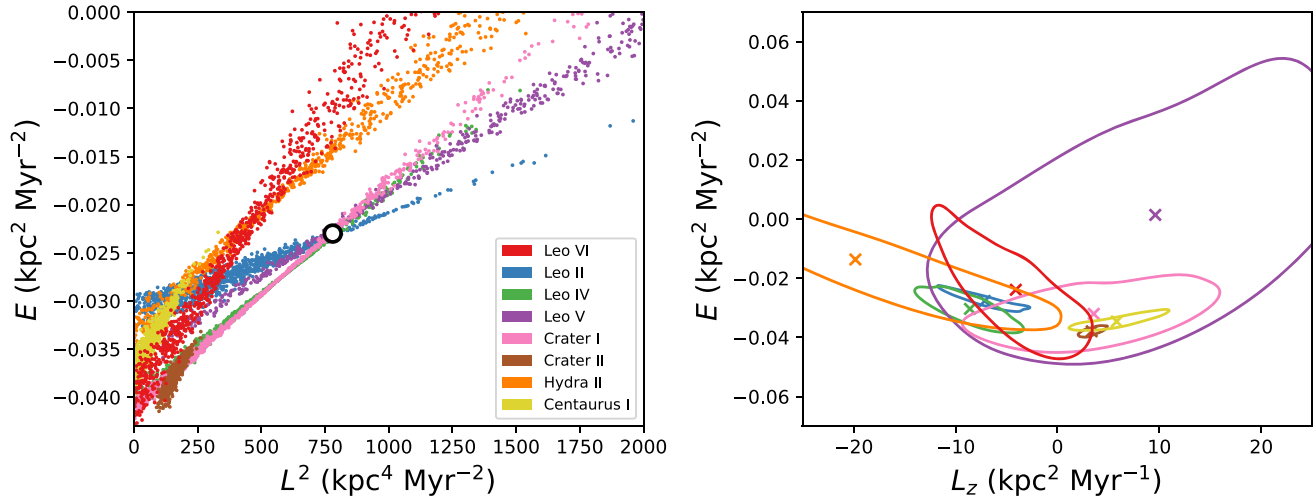

Figure 9. Left: the specific energy, E, vs. the square of the specific angular momentum, L^2, of Leo VI and the members of the Crater-Leo infall group. We find that the E–L^2 distributions of Leo II, Leo IV, Leo V, and Crater all intersect at (L^2, E) ∼ (780 kpc^4 Myr^{-2}, −0.023 kpc^2 Myr^{-2}), suggesting a common origin (M. S. Pawlowski 2021). The E–L^2 distribution of Leo VI is inconsistent with the other infall group members, suggesting that it may not be part of the group. Right: the specific energy, E, vs. the z-component of the specific angular momentum, L_z, of Leo VI and the other satellites. The cross markers represent the median E–L_z values of the satellites, while the contour lines represent the 1σ uncertainties. The E–L_z distribution of Leo VI is consistent with all the other members of the Crater-Leo infall group, albeit with large uncertainties.

E–L^2 distributions of Crater II, Leo VI, Hydra II, and Centaurus I are inconsistent with the other satellites of the group. However, as shown in Figure 9, the specific energy, E, and z-component of specific angular momentum E–L_z distribution of Leo VI is consistent with all the other members of the proposed group (including Crater II). Although this is mostly due to the large uncertainties in the proper motion measurement of Leo VI as Crater II has a inconsistent E–L_z distribution with some of the other members of the infall group such as Leo II and Leo IV.

Systems that are part of an infall group are also expected to have similar orbital poles or direction of angular momentum. M. P. Júlio et al. (2024) found that four systems in the proposed Crater-Leo Group (Leo II, Leo IV, Leo V, and Crater) have orbital poles that all intersect with each other, while positions of the orbital poles of Crater II do not match with the other members of the system. As shown in Figure 10, the position of the orbital pole of Leo VI is consistent with the group orbital pole of the Crater-Leo infall group at (α_{J2000}, δ_{J2000}) ∼ (210°, −24°) while Hydra II also has an orbital pole that is somewhat close by (∼6° away). As with the energy–angular momentum distributions, we find that position orbital pole of Centaurus I is inconsistent with the other members of the proposed group.

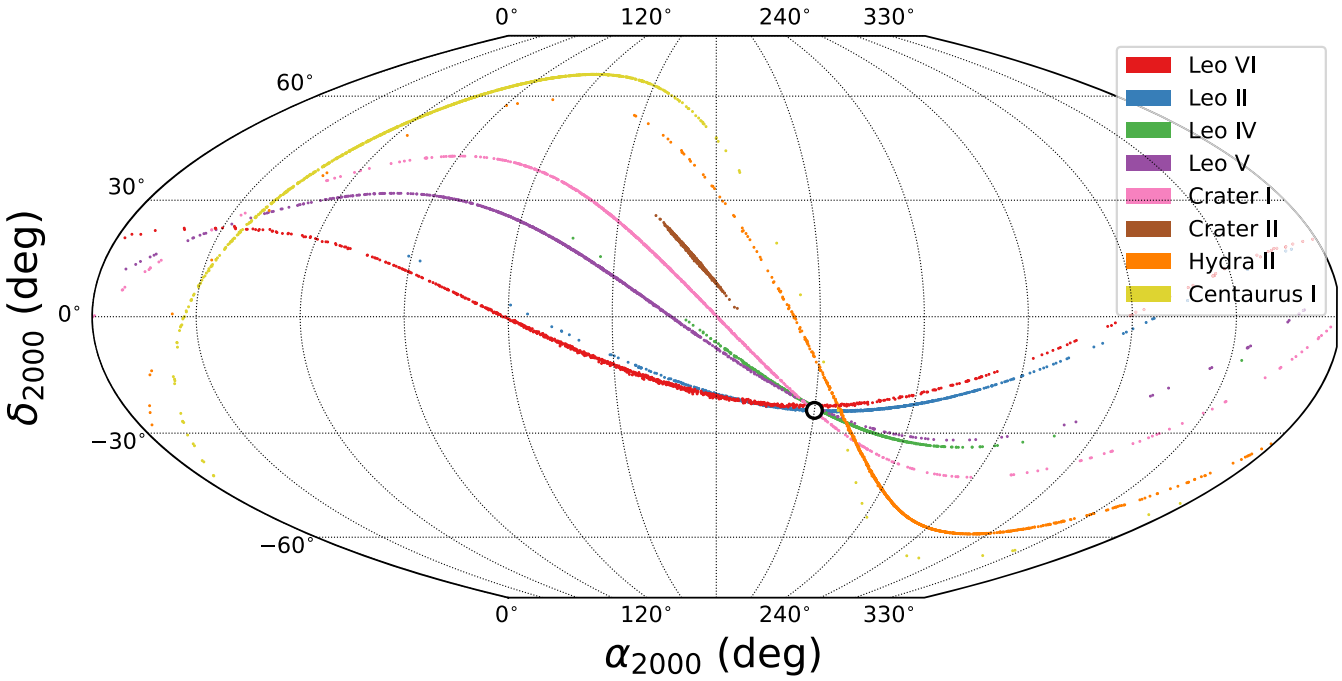

Figure 10. Distribution of the possible orbital poles of Leo VI and the other possible members of the Crater-Leo infall group. The position of the orbital pole of Leo VI is consistent with the possible group orbital pole of the Crater-Leo group (Leo II, Leo IV, Leo V, and Crater) at $(\alpha_{J2000}, \delta_{J2000}) \sim (210°, -24°)$, while the position of the orbital pole of Crater II is inconsistent with the group orbital pole.

While Leo VI shares a similar on-sky position, orbital pole location, and $E-L_z$ distribution with the members of the Crater-Leo infall group, due to its relatively close distance and inconsistent $E-L^2$ distribution with the other members of the group, we determine that it is unlikely for Leo VI being a part of the the proposed infall group. However, more precise measurements of the proper motion of Leo VI are needed to more definitely determine the its membership in the Crater-Leo group. Similarly, we also did not find convincing evidence that Leo Minor I, Hydrus II, and Centuarus I are part of the Crater-Leo infall group due to their inconsistent heliocentric distances, $E-L^2$ distributions, and orbital pole locations with the infall group.

6.4. Astrophysical J-factor

As mentioned in Section 1, MW satellite UFDs are also useful targets for searches for dark matter annihilation or decay products (M. Ackermann et al. 2015; A. Geringer-Sameth et al. 2015b; A. McDaniel et al. 2023; K. K. Boddy et al. 2024). The astrophysical component that governs the dark matter annihilation and decay fluxes are referred to as the J-factor and D-factor, respectively. Both factors depend on the dark matter density of the system along the line of sight such that $J(\theta) = \iint_{\rm los} \rho^2_{\rm DM} dl d\Omega$ and $D(\theta) = \iint_{\rm los} \rho_{\rm DM} dl d\Omega$, where $\rho_{\rm DM}$ is the dark matter density, dl is the line-of-sight direction, and $d\Omega$ is the solid angle with radius θ.

We use the framework developed by V. Bonnivard et al. (2015), A. Geringer-Sameth et al. (2015a), and A. B. Pace & L. E. Strigari (2019) to calculate the J-factor and D-factor of Leo VI. We model the system with a stellar component parameterized by a Plummer distribution (H. C. Plummer 1911) and dark matter component with a Navarro–Frenk–White profile (J. F. Navarro et al. 1997) while assuming a constant stellar anisotropy with radius. We then fit the dark matter profile by modeling the velocity dispersion of the member stars using the spherical Jeans equations and compared them with the measured velocity dispersion from the spectroscopic observations.

For the J-factor of Leo VI obtained using measurements from the nine member stars, we find $\log_{10} J(\theta) = 17.0^{+0.8}_{-1.0}$, $17.2^{+0.8}_{-1.0}$, $17.3^{+0.9}_{-1.0}$, and $17.3^{+0.9}_{-1.0}$ for solid angles of $\theta = 0.^\circ1$, $0.^\circ2$, $0.^\circ5$, and $1°$, respectively, in logarithmic units of GeV^2 cm^{-5}. These J-factor measurements are consistent with estimates of $\log_{10}(J(0.^\circ5)) = 16.9^{+0.8}_{-1.2}$, obtained from the empirical scaling relation derived in A. B. Pace & L. E. Strigari (2019):

$$\frac{J(0.^\circ5)}{\rm GeV^2\ cm^{-5}} = 10^{17.87}\left(\frac{\sigma_{\rm v,los}}{5\ {\rm km\ s^{-1}}}\right)^4 \times \left(\frac{D_\odot}{100\ {\rm kpc}}\right)^{-2}\left(\frac{R_{1/2}}{100\ {\rm pc}}\right)^{-1}. \quad (2)$$

For the D-factor of Leo VI, we find $\log_{10} D(\theta) = 16.6 \pm 0.5$, $17.0^{+0.5}_{-0.6}$, and $17.5\pm^{+0.6}_{-0.7}$, for solid angles of $\theta = 0.^\circ1$, $0.^\circ2$, and $0.^\circ5$, respectively, in logarithmic units of GeV cm^{-2}. As the velocity dispersion has a tail to zero velocity dispersion (see Figure A2), the J-factor and D-factor also have similar tails. We have applied a $V_{\rm max} > 1$ km s^{-1} cut to remove the tails and note that without this change the J-factor and D-factor both decrease by roughly 0.05 dex.

While Leo VI does not have a large J-factor compared to other MW UFDs, for example Wilman 1 and Ursa Major II have J-factors of $\log_{10} J(0.^\circ5) = 19.53^{+0.50}_{-0.50}$ and $19.44^{+0.41}_{-0.39}$ GeV^2 cm^{-5}, respectively (A. B. Pace & L. E. Strigari 2019), it could be included in a stacked analysis with other UFDs.

7. Summary

We have presented the DELVE EDR3 data set and used it to discover the MW satellite Leo VI. Using the `ugali` maximum-likelihood fit of the system's morphology and CMD, we

find that Leo VI is an old ($\tau > 12.37$ Gyr), metal-poor ($[\mathrm{Fe/H}]_{\mathrm{spec}} = -2.39^{+0.10}_{-0.13}$), stellar system with a low luminosity ($M_V = -3.56^{+0.47}_{-0.37}$ mag), large size ($R_{1/2} = 90^{+30}_{-30}$ pc), elliptical shape ($\epsilon = 0.54^{+0.19}_{-0.29}$), and a large heliocentric distance ($D = 111^{+9}_{-6}$ kpc). By obtaining Keck/DEIMOS spectroscopy of the possible member stars of Leo VI, we are able to find nine member stars and four candidate member stars for the system (with line-of-sight velocities of 155 km $\mathrm{s}^{-1} \leqslant v_{\mathrm{hel}} \leqslant 185$ km s^{-1}), and find a nonzero velocity dispersion of $2.85^{+1.57}_{-1.31}$ km s^{-1}. We are also able to obtain orbital properties of Leo VI by combining proper motion measurements from Gaia DR3 ($\mu_{\alpha *} = -0.06^{+0.18}_{-0.20}$ mas yr^{-1}, $\mu_{\delta} = -0.22^{+0.22}_{-0.17}$ mas yr^{-1}) with the system's measured radial velocity of $v_{\mathrm{hel}} = 170.03^{+1.75}_{-1.41}$ km s^{-1}.

Since their discovery in SDSS, there has been considerable uncertainty in the classification of some ultra-faint MW satellites as either UFDs or globular clusters (J. D. Simon 2019). As illustrated in Figure 5, the half-light radius of Leo VI ($R_{1/2} = 90^{+30}_{-30}$ pc) is bigger than all known MW globular clusters, likely indicating its identity as a UFD.

Compared to globular clusters, UFDs also have much higher amounts of dark matter (J. D. Simon 2019). If we assume that Leo VI is a self-gravitating star cluster, we can estimate the line-of-sight velocity using Equation (1) by assuming that the total mass within the half-light radius is half of the stellar mass. We thus estimate that if Leo VI's stars are self-gravitating, they would have a velocity dispersion of $\sigma_v \sim 0.2\,\mathrm{km\,s^{-1}}$. This is much lower than the measured dispersion of $2.85^{+1.57}_{-1.31}$ km s^{-1} further supporting the dark-matter-dominated nature of the system. We perform a Bayesian information criterion test and find that the self-gravitating model ($\sigma_v = 0.2\,\mathrm{km\,s^{-1}}$) is disfavored over the free σ_v parameter model at $\Delta_{\mathrm{BIC},01} = 4.8$, which approximately equivalent to a Bayes factor of 11.1 ($\mathrm{BF}_{10} \sim \exp(\Delta_{\mathrm{BIC},01}/2)$; R. E. Kass & A. E. Raftery 1995).

We also find a nonzero metallicity dispersion measurement of $\sigma_{[\mathrm{Fe/H}]} = 0.19^{+0.13}_{-0.11}$, which suggest the presence of a dark matter halo massive enough to retain the supernova ejecta needed for multiple generations of star formation (J. D. Simon 2019).

Despite the system's highly elliptical shape and the alignment of its proper motion vector with the semimajor axis, we have found that Leo VI's average density within its half-light radius is much larger than the average MW density at its orbital pericenter, disfavoring the idea that the system is undergoing disruption. The system also has an on-sky location that is close to other members of the proposed Crater-Leo infall group. However, it is improbable that Leo VI is a part of this group as its heliocentric distance and energy–angular momentum (E–L^2) distribution do not match the distribution found in other members.

Leo VI is the 14th ultra-faint MW satellite found in DELVE data (S. Mau et al. 2020; W. Cerny et al. 2021a, 2021b, 2023a, 2023b, 2023c, 2025). However, unlike the other DELVE satellites, it was found in the preliminary data from the DELVE EDR3 catalog, which features deeper and more accurate photometric measurements than previous DELVE releases (A. Drlica-Wagner et al. 2022). Therefore, it is expected that a more comprehensive dwarf galaxy search of the upcoming full DELVE DR3 catalog will yield many more new MW satellite discoveries. V. Manwadkar & A. V. Kravtsov (2022) forecasted that the final DELVE–WIDE survey is expected to find 64^{+17}_{-13} MW satellites with $M_V < 0$ and $R_{1/2} > 10$ pc at $\delta_{\mathrm{J2000}} < 0°$, while only 35 systems have been discovered in this region so far.[34] Furthermore, it is expected that the upcoming Vera C. Rubin Observatory's LSST (Ž. Ivezić et al. 2019) will discover hundreds of UFDs in the Local Volume (J. R. Hargis et al. 2014; B. Mutlu-Pakdil et al. 2021; V. Manwadkar & A. V. Kravtsov 2022). Space-based telescopes such as Roman (D. Spergel et al. 2015) and Euclid (Euclid Collaboration et al. 2022) are also expected to have the potential of finding more UFD galaxies (E. O. Nadler et al. 2024). This growing population of known UFDs in the Local Group will allow us to probe the matter power spectrum to even smaller scales and provide insight into the process of galaxy formation for the smallest galaxies.

Acknowledgments

We thank the anonymous referee for the many useful comments that helped us improve this manuscript. The follow-up DECam observations taken on 2023 June were obtained during a time trade with the Dark Energy Camera Legacy Survey (DECaLS) team. We note that Leo VI was also independently identified as a possible UFD among ∼300 candidates reported in an unpublished search of PS1 data by C. J. Grillmair (2018).

C.Y.T. was supported by the U.S. National Science Foundation (NSF) through the grants AST-2108168 and AST-2307126. W.C. thanks Michael Lundquist and the staff of the W.M. Keck Observatory for extensive assistance on the night of our Keck observations, and acknowledges support from a Gruber Science Fellowship at Yale University. A.B.P. acknowledges support from NSF grant AST-1813881. J.A.C.-B. acknowledges support from FONDECYT Regular N 1220083. C.E.M.-V. is supported by the international Gemini Observatory, a program of NSF NOIRLab, which is managed by the Association of Universities for Research in Astronomy (AURA) under a cooperative agreement with the U.S. National Science Foundation, on behalf of the Gemini partnership of Argentina, Brazil, Canada, Chile, the Republic of Korea, and the United States of America. G.E. M. acknowledges support from the University of Toronto Arts & Science Postdoctoral Fellowship program, the Dunlap Institute, and the Natural Sciences and Engineering Research Council of Canada (NSERC) through grant RGPIN-2022-04794. D.J.S. acknowledges support from NSF grant AST-2205863.

The DELVE project is partially supported by Fermilab LDRD project L2019-011, the NASA Fermi Guest Investigator Program Cycle 9 grant 91201, and the U.S. National Science Foundation (NSF) under grants AST-2108168 and AST-2307126. This work is supported by the Fermilab Visiting Scholars Award Program from the Universities Research Association. This material is also based upon work supported by the National Science Foundation Graduate Research Fellowship Program under grant No. DGE2139841. Any opinions, findings, and conclusions or recommendations expressed in this material are those of the author(s) and do not necessarily reflect the views of the National Science Foundation.

This project used data obtained with the Dark Energy Camera (DECam), which was constructed by the Dark Energy Survey (DES) collaboration. Funding for the DES Projects has

[34] The DELVE–WIDE survey has subsequently expanded coverage to $\delta_{\mathrm{J2000}} \lesssim 30°$.

been provided by the US Department of Energy, the U.S. National Science Foundation, the Ministry of Science and Education of Spain, the Science and Technology Facilities Council of the United Kingdom, the Higher Education Funding Council for England, the National Center for Supercomputing Applications at the University of Illinois at Urbana-Champaign, the Kavli Institute for Cosmological Physics at the University of Chicago, Center for Cosmology and Astro-Particle Physics at the Ohio State University, the Mitchell Institute for Fundamental Physics and Astronomy at Texas A&M University, Financiadora de Estudos e Projetos, Fundação Carlos Chagas Filho de Amparo à Pesquisa do Estado do Rio de Janeiro, Conselho Nacional de Desenvolvimento Científico e Tecnológico and the Ministério da Ciência, Tecnologia e Inovação, the Deutsche Forschungsgemeinschaft and the Collaborating Institutions in the Dark Energy Survey. The Collaborating Institutions are Argonne National Laboratory, the University of California at Santa Cruz, the University of Cambridge, Centro de Investigaciones Enérgeticas, Medioambientales y Tecnológicas–Madrid, the University of Chicago, University College London, the DES-Brazil Consortium, the University of Edinburgh, the Eidgenössische Technische Hochschule (ETH) Zürich, Fermi National Accelerator Laboratory, the University of Illinois at Urbana-Champaign, the Institut de Ciències de l'Espai (IEEC/CSIC), the Institut de Física d'Altes Energies, Lawrence Berkeley National Laboratory, the Ludwig-Maximilians Universität München and the associated Excellence Cluster Universe, the University of Michigan, NSF NOIRLab, the University of Nottingham, the Ohio State University, the OzDES Membership Consortium, the University of Pennsylvania, the University of Portsmouth, SLAC National Accelerator Laboratory, Stanford University, the University of Sussex, and Texas A&M University.

This work was possible based on observations at NSF Cerro Tololo Inter-American Observatory, NSF NOIRLab (NOIRLab Prop. ID 2019A-0305; PI: Alex Drlica-Wagner), which is managed by the Association of Universities for Research in Astronomy (AURA) under a cooperative agreement with the U.S. National Science Foundation.

Some of the data presented herein were obtained at Keck Observatory, which is a private 501(c)3 nonprofit organization operated as a scientific partnership among the California Institute of Technology, the University of California, and the National Aeronautics and Space Administration. The Observatory was made possible by the generous financial support of the W. M. Keck Foundation.

The authors wish to recognize and acknowledge the very significant cultural role and reverence that the summit of Maunakea has always had within the Native Hawaiian community. We are most fortunate to have the opportunity to conduct observations from this mountain.

This work has made use of data from the European Space Agency (ESA) mission Gaia (https://www.cosmos.esa.int/gaia), processed by the Gaia Data Processing and Analysis Consortium (DPAC; https://www.cosmos.esa.int/web/gaia/dpac/consortium). Funding for the DPAC has been provided by national institutions, in particular the institutions participating in the Gaia Multilateral Agreement.

This work has made use of the Local Volume Database (https://github.com/apace7/local_volume_database; A. B. Pace 2024).

This manuscript has been authored by Fermi Research Alliance, LLC, under contract No. DE-AC02-07CH11359 with the US Department of Energy, Office of Science, Office of High Energy Physics. The United States Government retains and the publisher, by accepting the article for publication, acknowledges that the United States Government retains a nonexclusive, paid-up, irrevocable, worldwide license to publish or reproduce the published form of this manuscript, or allow others to do so, for United States Government purposes.

Facilities: Blanco, Keck:II, and Gaia.

Software: `astropy` (Astropy Collaboration et al. 2013, 2018), `corner` (D. Foreman-Mackey 2016), `emcee` (D. Foreman-Mackey et al. 2013), `gala` (A. M. Price-Whelan 2017), `healpix` (K. M. Górski et al. 2005), `jupyter` (T. Kluyver et al. 2016), `matplotlib` (J. D. Hunter 2007), `numpy` (T. E. Oliphant 2015), `pandas` (W. McKinney 2010), `scipy` (P. Virtanen et al. 2020), `simple` (K. Bechtol et al. 2015), `skyproj` (https://github.com/LSSTDESC/skyproj), and `ugali` (K. Bechtol et al. 2015; A. Drlica-Wagner et al. 2021).

Appendix
Posterior Distributions of the Leo VI Parameters

In Figure A1, we present the posterior distributions of a simultaneous fit to Leo VI's morphological and isochrone properties derived from follow-up DECam observations of the system using `ugali`, as described in Section 4. The posterior was sampled with `emcee` using 40 walkers over 3000 steps, following an initial burn in of 1000 steps.

We present the posterior probability distributions for Leo VI's heliocentric radial velocity, $v_{\rm hel}$, and velocity dispersion, σ_v (Figure A2) and the distributions for its spectroscopic metallicity, $[{\rm Fe/H}]_{\rm spec}$, and metallicity dispersion, $\sigma_{\rm [Fe/H]}$ (Figure A3), obtained using data from the DEIMOS observation of the system (see Section 5).

Figure A4 shows the distribution of Leo VI's systematic proper motion and orbital parameters estimated from Gaia proper motion measurements of Leo VI's member stars (Section 6.1).

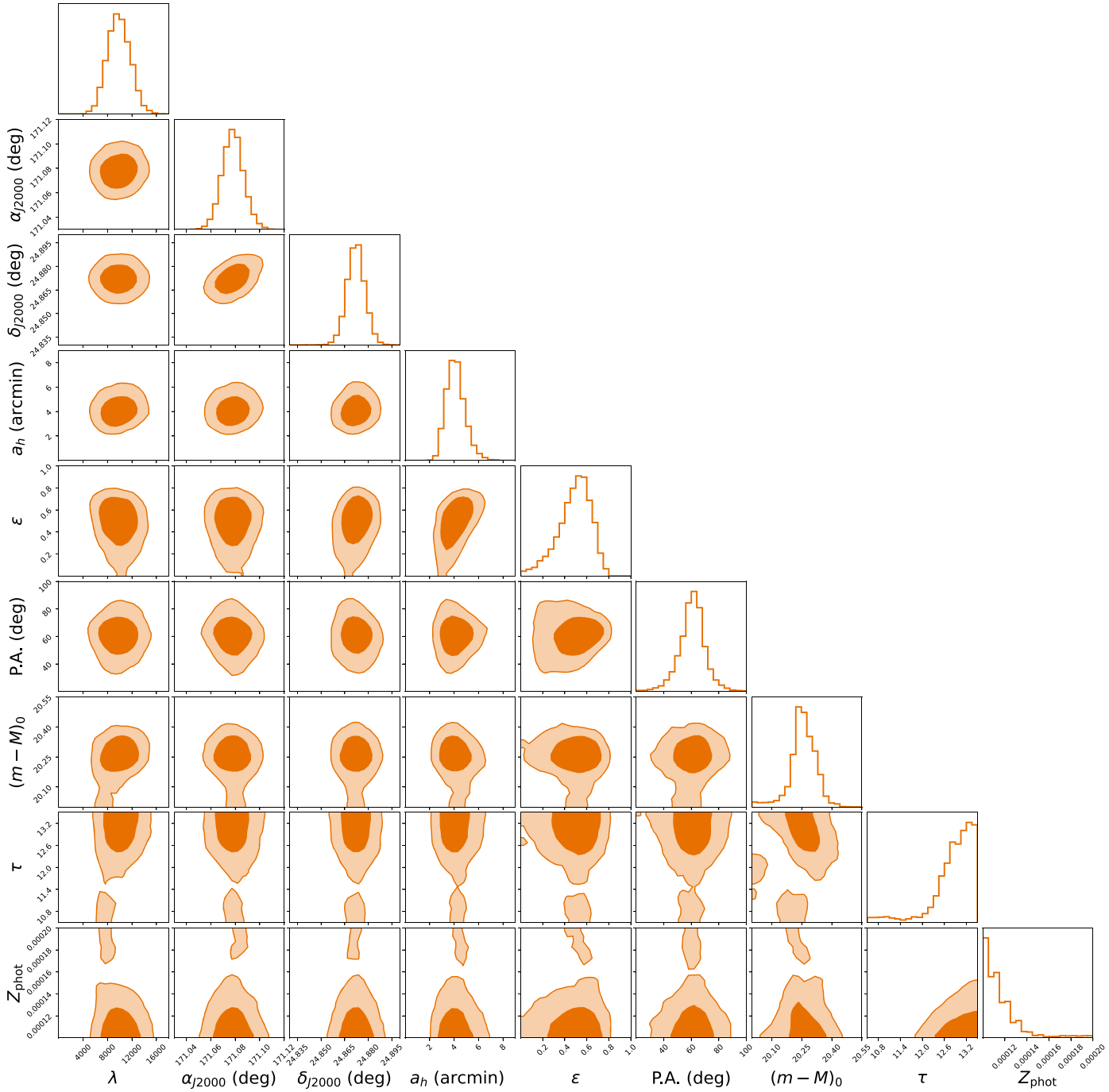

Figure A1. The posterior distributions of Leo VI's morphological and isochrone properties modeled using `ugali`. We simultaneously fit the system's stellar richness (λ), centroid coordinates (α_{J2000}, δ_{J2000}), angular semimajor axis length (a_h), ellipticity (ϵ), PA of the major axis, distance modulus ($(m-M)_0$), age (τ), and metallicity (Z_{phot}).

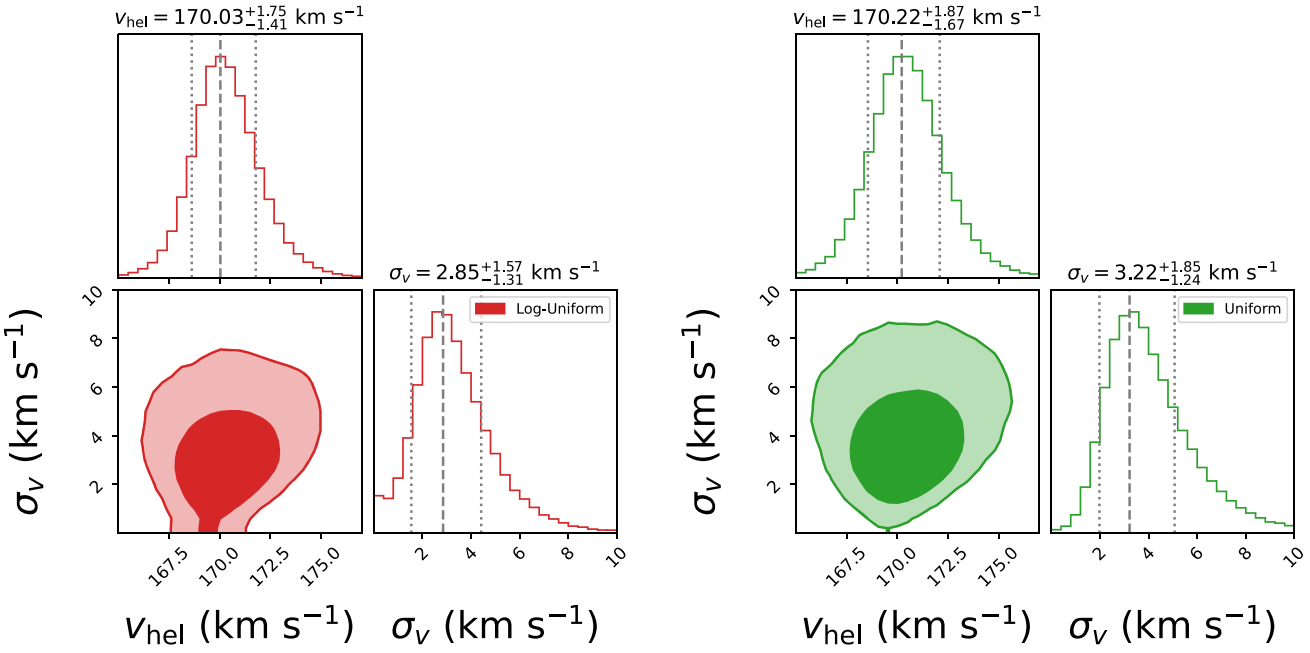

Figure A2. The posterior probability distributions for the systemic heliocentric radial velocity, v_{hel}, and velocity dispersion, σ_v, of Leo VI derived using Markov Chain Monte Carlo sampling. The left plot shows values obtained using a log-uniform prior while the right plot shown alternative values obtained using a uniform prior.

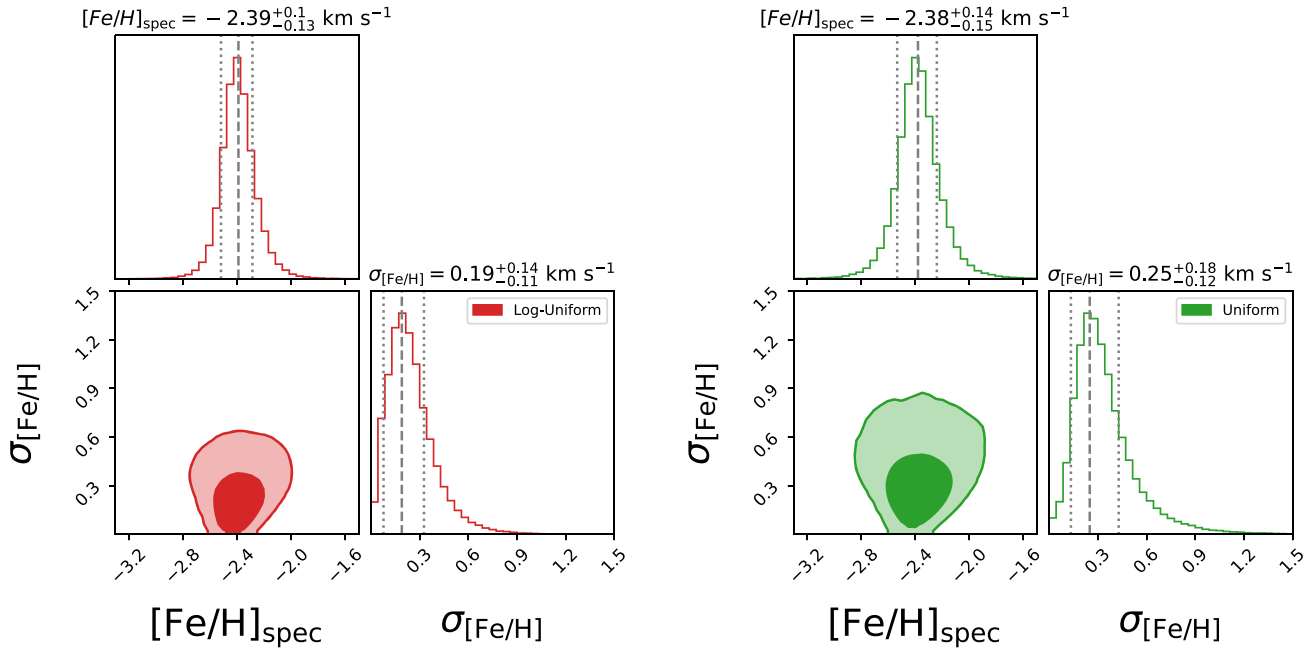

Figure A3. The posterior probability distributions for the spectroscopic metallicity, $[Fe/H]_{spec}$, and metallicity dispersion, $\sigma_{[Fe/H]}$, of the system. The left plot shows values obtained using a log-uniform prior while the right plot shown alternative values obtained using a uniform prior.

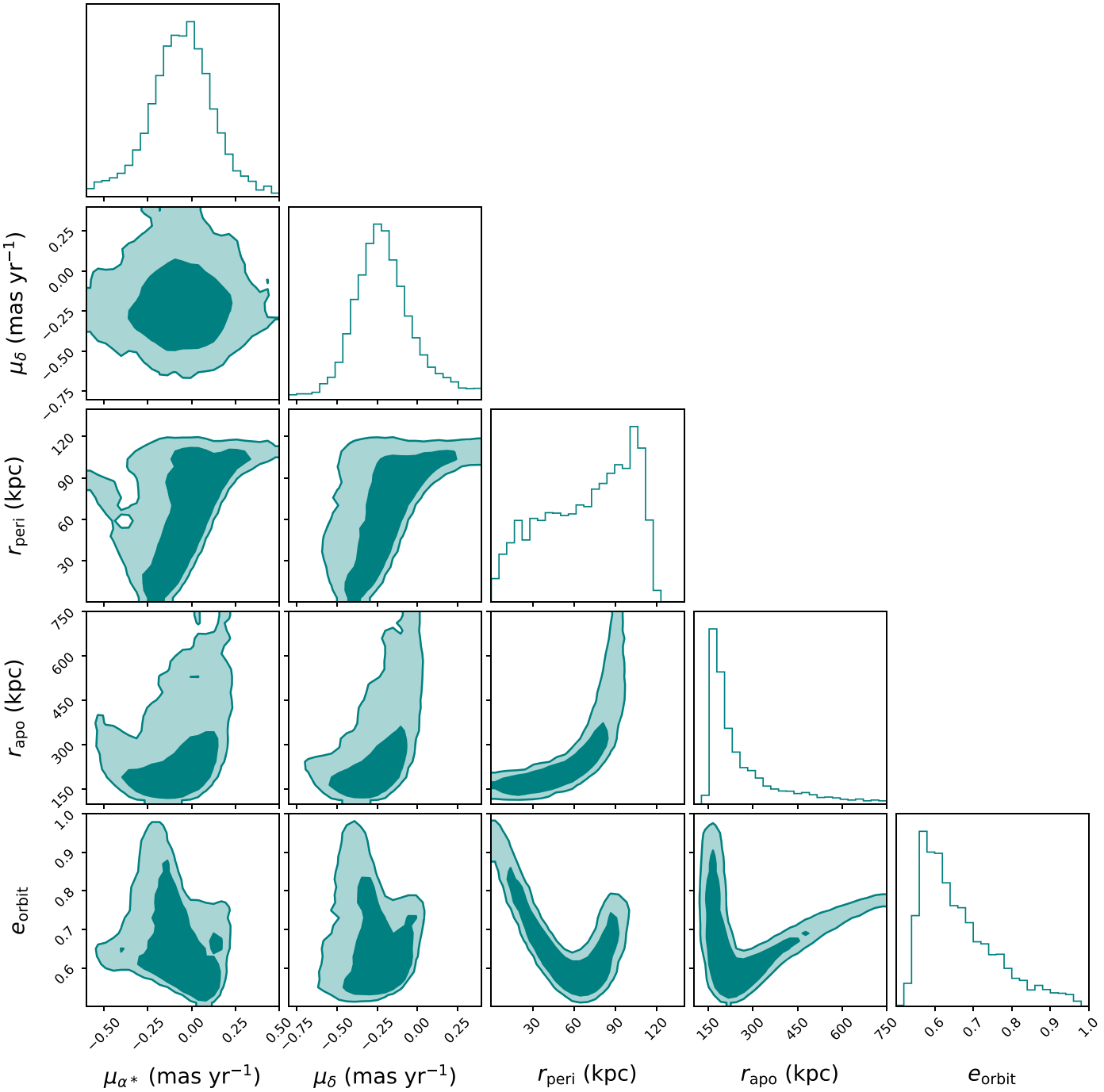

Figure A4. The distributions of Leo VI's systematic proper motion and orbital parameters. The systematic proper motion ($\mu_{\alpha*}$, μ_δ) were obtained from the proper motion measurements of Leo VI's member stars using a Gaussian mixture model sampled with `emcee`. While the orbital properties such as apocenter ($r_{\rm apo}$), pericenter ($r_{\rm peri}$), and eccentricity ($e_{\rm orbit}$) were obtained using `gala` with the distribution of the present-day 6D position and velocities obtained by sampling the posterior distribution of the system's observed parameters.

ORCID iDs

C. Y. Tan https://orcid.org/0000-0003-0478-0473
W. Cerny https://orcid.org/0000-0003-1697-7062
A. Drlica-Wagner https://orcid.org/0000-0001-8251-933X
A. B. Pace https://orcid.org/0000-0002-6021-8760
M. Geha https://orcid.org/0000-0002-7007-9725
A. P. Ji https://orcid.org/0000-0002-4863-8842
T. S. Li https://orcid.org/0000-0002-9110-6163
M. Adamów https://orcid.org/0000-0002-6904-359X
D. Anbajagane https://orcid.org/0000-0003-3312-909X
C. R. Bom https://orcid.org/0000-0003-4383-2969
J. A. Carballo-Bello https://orcid.org/0000-0002-3690-105X
J. L. Carlin https://orcid.org/0000-0002-3936-9628
C. Chang https://orcid.org/0000-0002-7887-0896
A. Chaturvedi https://orcid.org/0000-0001-5143-1255
A. Chiti https://orcid.org/0000-0002-7155-679X
Y. Choi https://orcid.org/0000-0003-1680-1884
M. L. M. Collins https://orcid.org/0000-0002-1693-3265
A. Doliva-Dolinsky https://orcid.org/0000-0001-9775-9029
P. S. Ferguson https://orcid.org/0000-0001-6957-1627

R. A. Gruendl https://orcid.org/0000-0002-4588-6517
D. J. James https://orcid.org/0000-0001-5160-4486
G. Limberg https://orcid.org/0000-0002-9269-8287
M. Navabi https://orcid.org/0000-0001-9438-5228
D. Martínez-Delgado https://orcid.org/0000-0003-3835-2231
C. E. Martínez-Vázquez https://orcid.org/0000-0002-9144-7726
G. E. Medina https://orcid.org/0000-0003-0105-9576
B. Mutlu-Pakdil https://orcid.org/0000-0001-9649-4815
D. L. Nidever https://orcid.org/0000-0002-1793-3689
N. E. D. Noël https://orcid.org/0000-0002-8282-469X
A. H. Riley https://orcid.org/0000-0001-5805-5766
J. D. Sakowska https://orcid.org/0000-0002-1594-1466
D. J. Sand https://orcid.org/0000-0003-4102-380X
J. Sharp https://orcid.org/0009-0001-1133-5047
G. S. Stringfellow https://orcid.org/0000-0003-1479-3059
C. Tolley https://orcid.org/0009-0007-0636-8876
D. L. Tucker https://orcid.org/0000-0001-7211-5729
A. K. Vivas https://orcid.org/0000-0003-4341-6172

References

Abbott, T. M. C., Adamów, M., Aguena, M., et al. 2021, ApJS, 255, 20
Ackermann, M., Albert, A., Anderson, B., et al. 2015, PhRvL, 115, 231301
Antilogus, P., Astier, P., Doherty, P., Guyonnet, A., & Regnault, N. 2014, JInst, 9, C03048
Arroyo-Polonio, J. M., Battaglia, G., Thomas, G. F., et al. 2023, A&A, 677, A95
Astropy Collaboration, Price-Whelan, A. M., Sipőcz, B. M., et al. 2018, AJ, 156, 123
Astropy Collaboration, Robitaille, T. P., Tollerud, E. J., et al. 2013, A&A, 558, A33
Bechtol, K., Drlica-Wagner, A., Balbinot, E., & Pieres 2015, ApJ, 807, 50
Belokurov, V., Walker, M. G., Evans, N. W., et al. 2008, ApJL, 686, L83
Belokurov, V., Zucker, D. B., Evans, N. W., et al. 2007, ApJ, 654, 897
Bernstein, G. M., Abbott, T. M. C., Desai, S., et al. 2017, PASP, 129, 114502
Bertin, E. 2006, in ASP Conf. Ser. 351, Astronomical Data Analysis Software and Systems XV, ed. C. Gabriel et al. (San Francisco, CA: ASP), 112
Bertin, E. 2011, in ASP Conf. Ser. 442, Astronomical Data Analysis Software and Systems XX, ed. I. N. Evans et al. (San Francisco, CA: ASP), 435
Bertin, E., & Arnouts, S. 1996, A&AS, 117, 393
Bertin, E., Mellier, Y., Radovich, M., et al. 2002, in ASP Conf. Ser. 281, Astronomical Data Analysis Software and Systems XI, ed. D. A. Bohlender, D. Durand, & T. H. Handley (San Francisco, CA: ASP), 228
Boddy, K. K., Carter, Z. J., Kumar, J., et al. 2024, PhRvD, 109, 103007
Bonnivard, V., Combet, C., Daniel, M., et al. 2015, MNRAS, 453, 849
Bovy, J. 2015, ApJS, 216, 29
Brandt, T. D. 2016, ApJL, 824, L31
Bressan, A., Marigo, P., Girardi, L., et al. 2012, MNRAS, 427, 127
Bullock, J. S., & Boylan-Kolchin, M. 2017, ARA&A, 55, 343
Carrera, R., Pancino, E., Gallart, C., & del Pino, A. 2013, MNRAS, 434, 1681
Catelan, M., & Smith, H. A. 2015, Pulsating Stars (New York: Wiley)
Cerny, W., Chiti, A., Geha, M., et al. 2025, ApJ, 979, 165
Cerny, W., Drlica-Wagner, A., Li, T. S., et al. 2023a, ApJL, 953, L21
Cerny, W., Martínez-Vázquez, C. E., Drlica-Wagner, A., et al. 2023b, ApJ, 953, 1
Cerny, W., Pace, A. B., Drlica-Wagner, A., et al. 2021a, ApJL, 920, L44
Cerny, W., Pace, A. B., Drlica-Wagner, A., et al. 2021b, ApJ, 910, 18
Cerny, W., Simon, J. D., Li, T. S., et al. 2023c, ApJ, 942, 111
Chambers, K. C., Magnier, E. A., Metcalfe, N., et al. 2016, arXiv:1612.05560
Chen, Y., Bressan, A., Girardi, L., et al. 2015, MNRAS, 452, 1068
Chen, Y., Girardi, L., Bressan, A., et al. 2014, MNRAS, 444, 2525
Clementini, G., Ripepi, V., Garofalo, A., et al. 2023, A&A, 674, A18
Dark Energy Survey Collaboration, Abbott, T., Abbott, T., et al. 2016, MNRAS, 460, 1270
Dey, A., Schlegel, D. J., Lang, D., et al. 2019, AJ, 157, 168
Drlica-Wagner, A., Bechtol, K., Mau, S., et al. 2020, ApJ, 893, 47
Drlica-Wagner, A., Bechtol, K., Rykoff, E. S., et al. 2015, ApJ, 813, 109
Drlica-Wagner, A., Carlin, J. L., Nidever, D. L., et al. 2021, ApJS, 256, 2
Drlica-Wagner, A., Ferguson, P. S., Adamów, M., et al. 2022, ApJS, 261, 38
Euclid Collaboration, Scaramella, R., Amiaux, J., et al. 2022, A&A, 662, A112
Everett, S., Yanny, B., Kuropatkin, N., et al. 2022, ApJS, 258, 15
Faber, S. M., Phillips, A. C., Kibrick, R. I., et al. 2003, Proc. SPIE, 4841, 1657
Flaugher, B., Diehl, H. T., Honscheid, K., et al. 2015, AJ, 150, 150
Foreman-Mackey, D. 2016, JOSS, 1, 24
Foreman-Mackey, D., Hogg, D. W., Lang, D., & Goodman, J. 2013, PASP, 125, 306
Fu, S. W., Weisz, D. R., Starkenburg, E., et al. 2023, ApJ, 958, 167
Gaia Collaboration, Brown, A. G. A., Vallenari, A., et al. 2018, A&A, 616, A1
Gaia Collaboration, Vallenari, A., Brown, A. G. A., et al. 2023, A&A, 674, A1
Geringer-Sameth, A., Koushiappas, S. M., & Walker, M. 2015a, ApJ, 801, 74
Geringer-Sameth, A., Koushiappas, S. M., & Walker, M. G. 2015b, PhRvD, 91, 083535
Górski, K. M., Hivon, E., Banday, A. J., et al. 2005, ApJ, 622, 759
Grillmair, C. J. 2018, Workshop:Near-Field Cosmology with the Dark Energy Survey's DR1 and Beyond, ed. T. Li, J. Bovy, & J. Carlin (Chicago, IL: Univ. Chicago Press), 11
Gruen, D., Bernstein, G. M., Jarvis, M., et al. 2015, JInst, 10, C05032
Gullikson, K., Dodson-Robinson, S., & Kraus, A. 2014, AJ, 148, 53
Hargis, J. R., Willman, B., & Peter, A. H. G. 2014, ApJL, 795, L13
Harrington, R. G., & Wilson, A. G. 1950, PASP, 62, 118
Hartley, W. G., Choi, A., Amon, A., et al. 2022, MNRAS, 509, 3547
Heiger, M. E., Li, T. S., Pace, A. B., et al. 2024, ApJ, 961, 234
Hunter, J. D. 2007, CSE, 9, 90
Husser, T. O., Wende-von Berg, S., Dreizler, S., et al. 2013, A&A, 553, A6
Hyndman, R. J. 1996, The American Statistician, 50, 120
Ivezić, Ž., Kahn, S. M., Tyson, J. A., et al. 2019, ApJ, 873, 111
Jarvis, M., Sheldon, E., Zuntz, J., et al. 2016, MNRAS, 460, 2245
Júlio, M. P., Pawlowski, M. S., Sohn, S. T., et al. 2024, A&A, 687, A212
Jurić, M., Kantor, J., Lim, K. T., et al. 2017, in ASP Conf. Ser. 512, Astronomical Data Analysis Software and Systems XXV, ed. N. P. F. Lorente, K. Shortridge, & R. Wayth (San Francisco, CA: ASP), 279
Kaplinghat, M., Tulin, S., & Yu, H.-B. 2016, PhRvL, 116, 041302
Kass, R. E., & Raftery, A. E. 1995, JASA, 90, 773
Kent, S. M. 2013, FERMILAB-SLIDES-20-114-SCD, Fermi National Accelerator Laboratory
Kirby, E. N., Cohen, J. G., Guhathakurta, P., et al. 2013, ApJ, 779, 102
Kirby, E. N., Simon, J. D., & Cohen, J. G. 2015, ApJ, 810, 56
Kluyver, T., Ragan-Kelley, B., Pérez, F., et al. 2016, in Positioning and Power in Academic Publishing: Players, Agents and Agendas, ed. F. Loizides & B. Schmidt (Amsterdam: IOS Press), 87
Koposov, S. E., Belokurov, V., Torrealba, G., & Evans, N. W. 2015, ApJ, 805, 130
Laevens, B. P. M., Martin, N. F., Bernard, E. J., et al. 2015, ApJ, 813, 44
Li, Y.-S., & Helmi, A. 2008, MNRAS, 385, 1365
Lovell, M. R., Frenk, C. S., Eke, V. R., et al. 2014, MNRAS, 439, 300
Lynden-Bell, D., & Lynden-Bell, R. M. 1995, MNRAS, 275, 429
Manwadkar, V., & Kravtsov, A. V. 2022, MNRAS, 516, 3944
Martin, N. F., de Jong, J. T. A., & Rix, H.-W. 2008, ApJ, 684, 1075
Martin, N. F., Nidever, D. L., Besla, G., et al. 2015, ApJL, 804, L5
Martínez-Vázquez, C. E., Vivas, A. K., Gurevich, M., et al. 2019, MNRAS, 490, 2183
Mau, S., Cerny, W., Pace, A. B., et al. 2020, ApJ, 890, 136
McDaniel, A., Ajello, M., Karwin, C. M., et al. 2023, arXiv:2311.04982
McKinney, W. 2010, in Proc. 9th Python in Science Conf., ed. S. van der Walt & J. Millman (Austin, TX: SciPy), 56
Melchior, P., Sheldon, E., Drlica-Wagner, A., et al. 2016, A&C, 16, 99
Minor, Q. E., Pace, A. B., Marshall, J. L., & Strigari, L. E. 2019, MNRAS, 487, 2961
Morganson, E., Gruendl, R. A., Menanteau, F., et al. 2018, PASP, 130, 074501
Muñoz, R. R., Majewski, S. R., & Johnston, K. V. 2008, ApJ, 679, 346
Mutlu-Pakdil, B., Sand, D. J., Crnojević, D., et al. 2021, ApJ, 918, 88
Nadler, E. O., Gluscevic, V., Driskell, T., et al. 2024, ApJ, 967, 61
Navarro, J. F., Frenk, C. S., & White, S. D. M. 1997, ApJ, 490, 493
Neilsen, E., Bernstein, G., Gruendl, R., & Kent, S. 2016, FERMILAB-TM-2610-AE-CD, Fermi National Accelerator Laboratory
Oliphant, T. E. 2015, Guide to NumPy (2nd ed.; USA: CreateSpace Independent Publishing Platform)
Pace, A. B. 2024, arXiv:2411.07424
Pace, A. B., Erkal, D., & Li, T. S. 2022, ApJ, 940, 136
Pace, A. B., & Strigari, L. E. 2019, MNRAS, 482, 3480
Pawlowski, M. S. 2021, Galax, 9, 66
Peñarrubia, J., Ludlow, A. D., Chanamé, J., & Walker, M. G. 2016, MNRAS, 461, L72
Plummer, H. C. 1911, MNRAS, 71, 460
Price-Whelan, A. M. 2017, JOSS, 2, 388

Prochaska, J., Hennawi, J., Westfall, K., et al. 2020, JOSS, 5, 2308
Rocha, M., Peter, A. H. G., Bullock, J. S., et al. 2013, MNRAS, 430, 81
Schlafly, E. F., & Finkbeiner, D. P. 2011, ApJ, 737, 103
Schlafly, E. F., Finkbeiner, D. P., Schlegel, D. J., et al. 2010, ApJ, 725, 1175
Schlegel, D. J., Finkbeiner, D. P., & Davis, M. 1998, ApJ, 500, 525
Sesar, B., Hernitschek, N., Mitrovic, S., et al. 2018, yCat, 153, 204
Sheldon, E. S. 2014, MNRAS, 444, L25
Shipp, N., Panithanpaisal, N., Necib, L., et al. 2023, ApJ, 949, 44
Simon, J. D. 2019, ARA&A, 57, 375
Spergel, D., Gehrels, N., Baltay, C., et al. 2015, arXiv:1503.03757
Tang, J., Bressan, A., Rosenfield, P., et al. 2014, MNRAS, 445, 4287
Tonry, J. L., Denneau, L., Flewelling, H., et al. 2018, ApJ, 867, 105
Torrealba, G., Koposov, S. E., Belokurov, V., & Irwin, M. 2016, MNRAS, 459, 2370
Virtanen, P., Gommers, R., Oliphant, T. E., et al. 2020, NatMe, 17, 261
Walker, M. G., Mateo, M., Olszewski, E. W., et al. 2006, AJ, 131, 2114
Willman, B., Blanton, M. R., West, A. A., et al. 2005a, AJ, 129, 2692
Willman, B., Dalcanton, J. J., Martinez-Delgado, D., et al. 2005b, ApJL, 626, L85
Wolf, J., Martinez, G. D., Bullock, J. S., et al. 2010, MNRAS, 406, 1220
Zuntz, J., Sheldon, E., Samuroff, S., et al. 2018, MNRAS, 481, 1149
Zwicky, F. 1942, PhRv, 61, 489